AMERICAN UNIVERSITY OF BEIRUT

# USING XFEM TO ESTIMATE THE PERMEABILITY OF SHALES DURING HYDRAULIC FRACTURING OPERATION

by
MAHMOUD IMAD KHADIJEH

A thesis
submitted in partial fulfillment of the requirements
for the degree of Master of Engineering
to the Department of Civil and Environmental Engineering
of the Maroun Semaan Faculty of Engineering and Architecture
at the American University of Beirut

Beirut, Lebanon
April 2021

AMERICAN UNIVERSITY OF BEIRUT

# USING XFEM TO ESTIMATE THE PERMEABILITY OF SHALES DURING HYDRAULIC FRACTURING OPERATION

by

MAHMOUD IMAD KHADIJEH

Approved by:

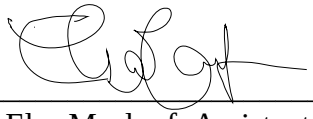

Dr. Elsa Maalouf, Assistant Professor — Advisor
Department of Chemical Engineering and Advanced Energy

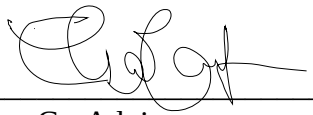

Dr. Alissar Yehya, Assistant Professor — Co-Advisor
Department of Civil and Environmental Engineering

Dr. George Saad, Associate Professor — Member of Committee
Department of Civil and Environmental Engineering

Dr. Shadi Najjar, Associate Professor — Member of Committee
Department of Civil and Environmental Engineering

Date of thesis defense: April 27, 2021

# AMERICAN UNIVERSITY OF BEIRUT

## THESIS RELEASE FORM

Student Name: Khadijeh Mahmoud Imad
Last First Middle

I authorize the American University of Beirut, to: (a) reproduce hard or electronic copies of my thesis; (b) include such copies in the archives and digital repositories of the University; and (c) make freely available such copies to third parties for research or educational purposes:

☐ As of the date of submission

☒ One year from the date of submission of my thesis.

☐ Two years from the date of submission of my thesis.

☐ Three years from the date of submission of my thesis.

Mahmoud Khadijeh May 8, 2021

Signature Date

# ACKNOWLEDGEMENTS

I would like to express my deep thanks and gratitude to my advisor Dr. Elsa Maalouf who supported me during my journey at AUB to accomplish this work. The meetings and comments that she provided during my work on this research have been helpful and have greatly improved my knowledge in the Geomechanics field.

A special thanks to my Co-advisor Dr. Alissar Yehya, for providing guidance, support, constructive feedback and for helping me with the validation of results.

I would like to express my gratitude to the committee members Dr. George Saad and Dr. Shadi Najjar for their constructive comments on my proposal, which helped me develop and improve my thesis.

I would also like to extend my deepest gratitude to my engineer friends, Dima Yassine and Hawraa Kareem for the moral support during my journey at AUB.

Finally, I acknowledge the IT department at AUB for their technical support.

# ABSTRACT
# OF THE THESIS OF

Mahmoud Imad Khadijeh for Master of Engineering
Major: Civil Engineering

Title: Using XFEM To Estimate the Permeability of Shales During Hydraulic Fracturing Operation

Hydraulic fracturing (HF) is used to increase the production of hydrocarbons from shale reservoirs by increasing shale permeability. In this work, we analyze the efficiency of hydraulic fracturing operations under various far-field stresses and injection rates, and we determine the effect of the degree of anisotropy on fracture propagation. Hydraulic fracturing of unconventional reservoirs is simulated using the coupled pressure/deformation extended finite element method (XFEM) in ABAQUS. We model the reservoir as a vertical transversely isotropic (VTI) medium with a degree of anisotropy that varies between 1 and 6, while the injection rate varies between 1E-5 to 1E-2 $m^3/s$. Multistage HF models are considered to compare the fractured area when applying close and wide cluster spacing. The numerical model is validated using the KGD model and three experimental studies available in the literature. We calculate the permeability of the fractured medium using the analytical model of Gueguen and Dienes, enhanced to account for the proppants' presence within the fractures using the Kozeny-Carmen equation. Our results show that the length and width of fractures, and the direction of the crack growth are strongly affected by the borehole stresses, the injection rate, and the degree of anisotropy. The cracks expand towards the maximum principal stress in the isotropic formation and kink towards the weakest plane in the VTI formation as the mechanical contrast exceeds 4 and when the injection rate is between 1E-4 and 1E-3 $m^3/s$. A decrease in the fracture aperture is observed for these cases. Moreover, crack propagation paths and geometries are affected by the far-field stresses when the distance between cracks is less than 12 m. However, cracks grow independently when the distance between the cracks exceeds 12 m (the beginning of a planar growth is observed), and a planar propagation is observed for a distance above 20 m. In multistage HF, the length, width, and extent of the fractured area are larger for close cluster spacing (<12m) than for high cluster spacing (>12m). This work allows the identification of the best fracturing scenario to optimally enhance the permeability of unconventional reservoirs under different hydro-mechanical conditions.

TABLE OF CONTENTS

# ILLUSTRATIONS

Figure

# TABLES

Table

# CHAPTER 1

# INTRODUCTION

## 1.1. Introduction

Hydraulic fracturing is a powerful technology that has been used for at least 60 years. More than 600 trillion cubic feet of natural gas and 7 billion barrels of oil have been produced using this technique (EIA, 2010) and up to 95% of new wells drilled today are hydraulically fractured, yielding more than 43% of the total U.S oil production (Perry, 2010). Hydraulic fracturing is used to produce natural gas from low permeable formations that are drilled horizontally. The operation starts by drilling a vertical wellbore until reaching the target reservoir where the well deviates and is drilled horizontally to increase the surface contact between the well and the hydrocarbon reservoir. The wellbore is cased, and perforations are created along the horizontal wellbore to inject a pressurized fluid and to fracture the intact rock. The type, composition, and amount of the fluids injected depend on the geological structure, the pore pressure, elastic properties, and heterogeneity of the target formation. This process is repeated along the entire length of the horizontal wellbore until the hydraulic fracturing treatments are finished. At the end, a permanent wellhead is installed at the surface so the oil and natural gas derived can be captured. Knowledge of the fracture dimensions (length/width/height), orientation, and wellbore pressure are essential for both the design and integrity of hydraulic fracturing field operations (Zielonka, et al. 2014). In addition, a good knowledge of the fracture geometry will help in the accurate estimation of the permeability which is one of the most fundamental properties required for modeling hydrocarbon production. No accurate technique for measuring the

geometries of fracture during or after the hydraulic fracturing process is currently available in the field. Even for their most simplistic forms, it is hard to establish direct solutions from the underlying differential equations that demonstrate the various physical processes occurring during fracking (Zielonka, et al. 2014). Therefore, the use of the numerical tools is recommended to reproduce fracking conditions that cannot be achieved in field fracturing such as, the variation of the far-field stresses, heterogeneity of the shale formation, the dip angle of beds, and the mechanical contrast between the layers.

### 1.2. Thesis Objective

Although numerous studies have shown that the spacing between the clusters has a considerable impact on the fracture opening and injection pressure in isotropic rocks, considering the rocks as vertical transversely isotropic (VTI) formations is critical, as the majority of unconventional reservoirs are anisotropic in nature. In formations with fine layering, the fractures propagate in the plane of least resistance, i.e., the plane with the smallest elastic properties. A nonplanar propagation that occurs in layered and heterogeneous formations yields high compression stress on the proppant within the cracks, which causes the proppants to be crushed and to flow back to the borehole when pressure is released. This causes the crack width to decrease (Maslowski, Kasza, and Wilk 2018). The direction of propagation of fractures is also affected by the far-field stresses and the distance between the clusters. Understanding these variables and identifying the parameters influencing crack geometry would result in greater permeability and conductivity, thus, contributing to higher production rates.

The aim of this research is to understand how the heterogeneities and anisotropy of shale formations and the injection strategies can constrain the hydraulic

fracturing (HF) propagation and affect the targeted permeability evolution. The effect of the injection rate, far-field stresses, and the mechanical contrast (MC) between the layers are examined using the extended finite element method (XFEM). We show the effect of cluster spacing and far-field stresses on the value of permeability following HF. Moreover, we study triple stages HF to examine the effect of the number of stages on fracture geometry and pore pressure.

### 1.3. Thesis Outlines

This report proceeds as follows. Chapter 2 includes a literature review about the hydraulic fracturing operation in addition to the parameters that affect the permeability. Chapter 3 describes the XFEM, the KGD analytical solution, Gueguen and Dienes analytical models, and the model construction. Chapter 4 shows the validations of the simulations using the KGD model and a set of experimental tests. Chapter 5 shows the results of the models for a single crack and triple clusters, including the sensitivity analysis on the injection rate, mechanical contrast (MC), cluster spacing, and multi-stage fracturing completion designs. Section 6 contains a discussion of the main observations.

# CHAPTER 2

# BACKGROUND AND LITERATURE

## 2.1. Literature Review

Hydraulic fracturing (HF) has become an increasingly important technique for producing oil and natural gas in places where hydrocarbons were previously inaccessible. Shale gas reservoirs, which are characterized by low permeability (order of nano-Darcy), contain a substantial amount of natural gas that can be recovered using HF. It is therefore important to characterize the initiation and propagation of the hydraulic fractures for efficient completion designs, to enhance reservoir permeability and avoid any undesirable propagation of fractures.

The efficiency of the HF process depends on the rock elastic properties and the degree of anisotropy. Sosa Massaro et al., (2017) performed triaxial compression tests and ultrasonic measurements on cores from the Vaca Muerta formation to calculate their elastic properties. Their results show that assuming an isotropic model to estimate the elastic properties of Vaca Muerta yield inefficient HF operations. Therefore, the shale rocks need to be modeled as vertical transverse isotropic (VTI) rocks to better characterize the fracture network and estimate the permeability. The degree of anisotropy of VTI reservoirs is key in describing the fracture pattern. AlTammar et al., (2019) conducted a HF test on layered samples with different mechanical properties. Their results indicate that the crack is oriented toward the weakest material (the material with the smallest elastic modulus), as the contrast in Young's modulus between the layers increases. In addition, they showed that the energy required for the fracture to develop is larger for a layered formation compared to the

case of an isotropic rock. The fracture path and geometry also depend on the presence of natural fractures (NF). Although the presence of NF is often neglected in the modeling of HF, NF is a major contributing factor to the enhancement of permeability during fracking. Rahimi-Aghdam et al., (2019) used the crack band model, in which crack deformation is smeared over the element width, to incorporate the impact of branching from the main fracture. They showed that the permeability is 10,000 times larger when taking into account the branching from the main fracture that occurs due to the presence of the NF.

Although it is well known that the HF propagates towards the minimum horizontal stress, it was shown that fracture initiation and propagation direction depend on the location and orientation of pre-existing fractures, weak planes, and the difference between the vertical and horizontal far-field stresses (Li, et al., 2019; Suarez-Rivera, et al., 2013). Other factors that influence the permeability of the reservoir after HF are the number and distances between the clusters and the number of HF stages. Early studies believed that for multi-cluster perforation in horizontal wells, the best cluster spacing is 20 m to 30 m (Modeland, Buller and Chong, 2011; XU et al., 2018) . If three clusters are used, the distance between HF stages is generally between 60 and 90 m. Hongjie Xiong, (2018) showed that the completion process is less effective when using a higher number of clusters per stage. He indicated that having a few clusters and more stages would increase the fractures' area, leading to effective completion, higher production rates, and faster pressure depletion.

Wang et al., (2016) investigated the effect of fluid injection rate by simulating the HF process in a formation modeled with a pre-existing discrete fracture network (DFN). They found that the main fractures (the hydraulic fractures) intersect with

secondary fractures (the DFN) when the injection rate ranges between 1E-4 and 4E-4 $m^3/s$, which leads to length of fractures to decrease. However, when the formation is homogenous (in the absence of NFs), the HFs propagate further under high injection rates (=4E-4 $m^3/s$).

Several methods are used to calculate the permeability of the fractures as a function of their length and width. For example, Sarkar, Toksoz and Burns, (2004) used the cubic law to calculate the permeability in terms of the fracture aperture. They found that if a fracture is inclined with respect to the axis of pressure gradient, then the value of the permeability ($K$) must be reduced by a factor of cosine of the inclination angle. Moreover, the Kozeny-Carman relation yields the values of the permeability in terms of empirical parameters and the porosity of the fracture region (Mavko, Mukerji and Dvorkin, 2009). Erol et al., (2017) developed a new non-empirical KC-type analytical model for predicting matrix and fracture permeability during single-phase flow. They indicated that if the grain size distribution of a matrix block is large, fluid flow occurs through the grains and fractures that have small hydraulic apertures and there is a minor influence on the permeability.

The numerical simulations offer the flexibility to change various parameters that improve the permeability of shale during HF operations. For example, the far-field stresses conditions of the reservoir, fluid injection rates, clusters spacing, number of stages. The finite element method (FEM) is an efficient and accurate method to model HF operations. For example, the cohesive zone model (CZM) is used to simulate HF and includes the material softening effects at the fracture tip, which simulates the quasi-brittle propagation of the fracture in shale rocks compared to ductile and brittle propagation in steel and glass (Haddad and Sepehrnoori, 2016). Moreover, the CZM is

employed to model the intersection of cracks during a multi-stage HF operation in conjunction with the effect of plasticity (Sobhaniaragh et al., 2019). The results obtained in (Sobhaniaragh et al., 2019) revealed that neglecting the plastic deformation in the HF simulations might lead to inaccurate predictions of fracture geometries and breakdown pressure. The main weakness of the CZM, however, is that the fracture propagation follows a predefined path called the cohesive layer. Therefore, this method cannot be used to predict the nonplanar propagation of fractures. The extended finite element method (XFEM) based on CZM outperforms the traditional CZM in predicting nonplanar fracture propagation. The crack propagates in unspecified pathways and independently of the mesh, as opposed to the conventional FEM. The primary advantage of the XFEM is that the finite element mesh does not need to be adjusted to map the crack path. Haddad and Sepehrnoori, (2016) used the XFEM to model one-stage multiple-cluster HF in quasi-brittle shale formations. They showed that the cluster spacing controls the crack opening as the opening of one fracture in the cluster causes the other fractures in the cluster to close. Wang, (2015) used the XFEM in conjunction with the Mohr Columb failure criteria to simulate the nonplanar HF propagation in a ductile formation. He showed that the plastic failure caused by HF propagation has a major effect on the pore pressure and fracture geometry. He indicated that if ductile formations are considered soft rocks, the prediction of fracture propagation path is inaccurate.

Previous work has shown that the spacing between the clusters affect the fracture width and the injection pressure in isotropic rocks (Haddad and Sepehrnoori, 2016). However, shale formations are layered and anisotropic. In formations with fine layering, the fractures propagate in the plane of least resistance, i.e., the plane with the

smallest elastic properties. A nonplanar propagation that occurs in layered and heterogeneous formations yields high compression stress on the proppant present within the cracks, which causes the proppants to be crushed and flow back to the borehole when pressure is released. This causes the crack width to decrease (Maslowski, Kasza and Wilk, 2018). The far-field stresses and the distance between the clusters also affect the direction of propagation of fractures. Identifying the parameters influencing crack geometry would result in an enhanced reservoir permeability, thus, contributing to higher production rates.

# CHAPTER 3

# METHODOLOGY

## 3.1. Introduction

Hydraulic fracturing modeling is governed using the Extended Finite Element Method (XFEM) governed by principles and laws. In this chapter, the theoretical background of the XFEM, traction separation law, fluid flow within the cohesive element are reviewed. The modifications made to Gueguen and Dienes method in calculating the permeability to include the presence of the proppant are then explained.

## 3.2. The Extended Finite Element Method (XFEM)

Belytschko and Black (1999) introduced the Extended Finite Element Method (XFEM) as an extension of the classical FEM based on the concept of partition of unity, which allows local enrichment functions to be easily incorporated into a finite element approximation. This method enables the modeling of discontinuities in the fluid pressure field as well as fluid flow within the cracked element surfaces (Smith et al., 2020). The discontinuities are controlled by special enriched functions combined with additional degrees of freedom, namely tip enriched nodes, Heaviside nodes, and fluid nodes (**Figure .1**). The XFEM thus allows the accurate approximation of fields within elements that include jumps, kinks, singularities, and other non-smooth characteristics without the need to update the finite element mesh and track the crack path. In the XFEM, the displacement vector function, $u$, is obtained by (Wang, 2015) :

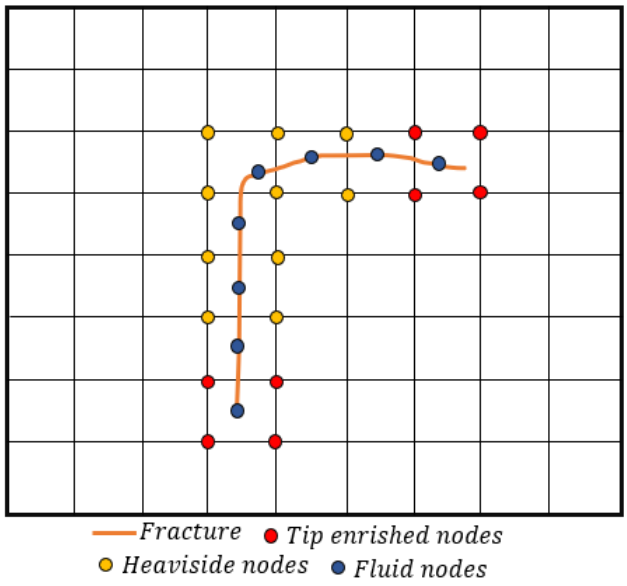


**Figure .1** A schematic of a single fracture (orange line) with enrichment elements on tips wall, and the common fluid nodes.

$$u = \sum_{I \in S_{all}} N_I(X)\, u_I \; + \sum_{I \in S_{frac}} N_I(X) H(x) a_I + \sum_{I \in S_{tip}} N_I(X) \sum_{l=1}^{4} F_a(x) b_I^l \,] \quad \ldots (1)$$

where $S_{all}$ is the set of all ordinary nodes, $S_{frac}$ and $S_{tip}$ are the set of Heaviside enrichment nodes and the set of fracture-tip enrichment nodes, respectively. $N_I(X)$ are the usual nodal shape functions. $u_I$ is the usual nodal displacement vector associated with the continues part of the regular finite element. $a_I$ and $b_I^l$ represent the enrichment nodal degrees of freedom for fracture and crack-tip, respectively. $H(x)$ is the enrichment shape jump function called the Heaviside function. $F_a$ is the singular displacement field around the facture tip. The function $H(x)$ is given by

$$H(x) = \begin{cases} 1 & if (x - x^*).n \geq 0 \\ -1 & otherwise \end{cases} \quad \ldots (2)$$

where $x$ is a sample (Gauss) point, $x^*$ is the point on the crack closest to $x$, and $n$ is the unit outward normal vector to the crack at $x^*$. $r$ and $\theta$ in **Figure .2** denote the local

polar coordinates system with its origin at the crack tip and $\theta = 0$ is tangent to the crack at the tip. The asymptotic crack tip function, $F_a(x)$ can be determined by (Wang, 2015):

$$F_a(x) = \left[\sqrt{r}\ sin\frac{\theta}{2}.\sqrt{r}\ cos\frac{\theta}{2}.\sqrt{r}\ sin\theta\ sin\frac{\theta}{2}.\sqrt{r}\ sin\theta\ cos\frac{\theta}{2}\right] \quad \ldots(3)$$

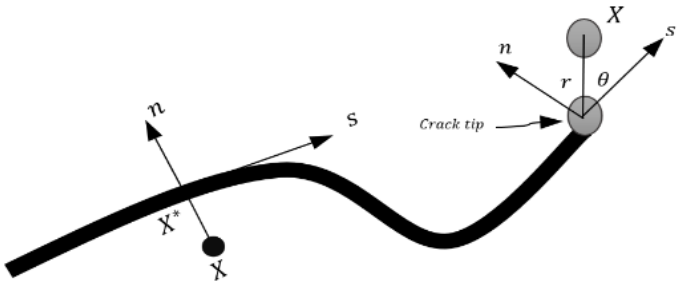


**Figure .2** Smooth crack with the normal and tangential coordinate system

### 3.3. Crack Initiation and Damage Evolution

The XFEM is very effective for modeling HF applications as the fracture will propagate arbitrarily and independently of the mesh. Moreover, the XFEM couples pore pressure stress diffusion with matrix deformation in the rock and allows arbitrary propagation of fractures while taking into account the fracture tip's viscosity (Li, et al., 2019). The crack in contact with fluid injection will initiate and propagate following the traction separation law. Several crack initiation criteria based on the traction separation law can be adopted in ABAQUS, namely, maximum principal stress (MAXPS), maximum principal strain (MAXPE), quadratic nominal strain damage (QUADE), and quadratic nominal stress damage (QUADS) (Smith, 2020). In this paper, the maximum principal stress is adopted to define the criteria for fracture initiation as follows:

$$f = \left\{\frac{\langle\sigma_{max}\rangle}{\sigma^0_{max}}\right\} \quad \ldots(4)$$

where $\sigma^0_{max}$ is the tensile strength. The symbol $\langle\ \rangle$ around $\sigma_{max}$ represents the Macaulay bracket, which is used to denote that a pure compressive stress does not

initiate damage. Equation (4) indicates that the crack will propagate when the stress ratio $f > 1$.

According to the traction separation law, when a load is applied, traction components will progressively increase to reach the full material limits in tension $T_n$ and shear $T_s$ (**Figure. 3**). After the load exceeds the material limit, a new crack will emerge at the crack edge causing a reduction in traction components (Maji, 2018). The instantaneous tractions in tension ($t_n$) and shear ($t_s$) are given by

$$t_n = (1 - D)T_n, \quad \text{where} \quad T_n = K_p \delta_n \qquad \dots (5)$$

$$t_s = (1 - D)T_s, \quad \text{where} \quad T_s = K_p \delta_s \qquad \dots (6)$$

where $T_n$ and $T_s$ are maximum traction limits for tension and shear, respectively. $\delta_n$ and $\delta_s$ are the relative displacements due to tension and shear tractions, respectively, acting on the predefined crack. $D$ is a scalar variable ranging between 0 and 1, and it is introduced to represent the average damage in the process of fracture propagation. The element is considered fully broken when $D = 1$. The variable $D$ is given by (Li, et al., 2019):

$$D = \frac{\delta_m^f (\delta_m^{max} - \delta_m^0)}{\delta_m^{max} (\delta_m^f - \delta_m^0)} \qquad \dots (7)$$

where $\delta_m^f$ is the mixed mode relative displacement that is observed at the complete failure. $\delta_m^{max}$ is the maximum value of the mixed mode relative displacement attained at that loading history and $\delta_m^0$ is the mixed mode relative displacement that is observed at the crack initiation. In this model, the Benzeggagh-Kenane fracture criterion (Benzeggagh and Kenane, 1996) is applied to describe the evolution of mixed-mode damage during fracture propagation. These criteria are appropriate for circumstances where the critical fracture energy is identical in the first and second shear directions of

rock material. The combined energy dissipated as a consequence of $G^c$ failure is introduced as follows (HanYi Wang, 2017) :

$$G^c = G_I^c + (G_{II}^c - G_I^c)\left(\frac{G_{Shear}}{G_{total}}\right)^{\eta}, \qquad \dots (8)$$

where $G_{Shear} = G_{II}^c + G_{III}^c$ and $G_{total} = G_{Shear} + G_I^c$. $G_I^c, G_{II}^c, G_{III}^c$ are the work done by the tractions and their conjugate relative displacements in the normal, first, and second shear directions, respectively. The traction-separation responses in different modes are assumed to be the same in this study, where $G_I^c = G_{II}^c$, so the cohesive response is insensitive to parameter $\eta$. The fracture will propagate when the energy release rate reaches the value of $G^c$. The newly introduced crack is always orthogonal to the maximum local tensile stress direction when the fracture criterion is met.

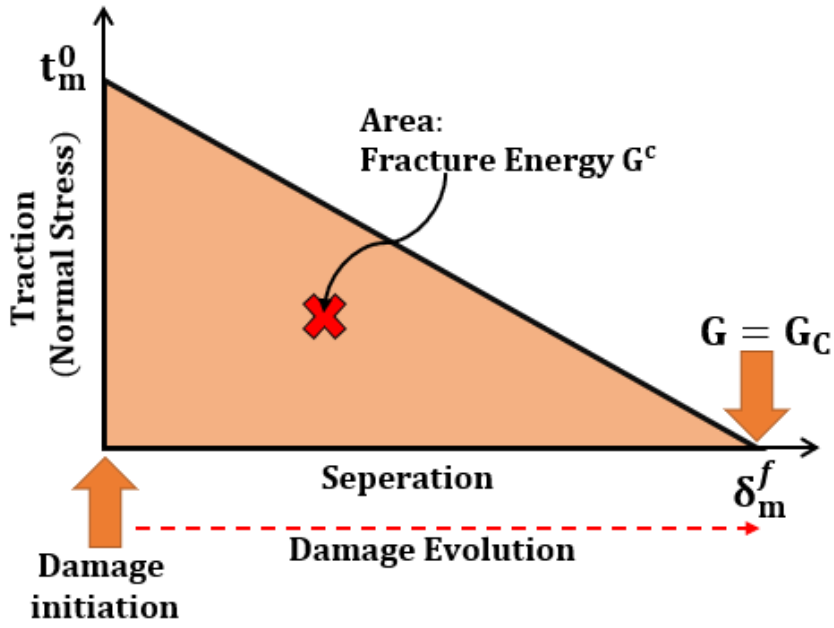


**Figure. 3** Traction separation law in the XFEM and the damage evolution

### 3.4. Fluid Flow within CZM

Two types of flow are observed within the elements intersecting the fracture (**Figure. 4**). The first type is the local tangential flow between two parallel plates $q_f$**.** It can be determined by the pressure gradient to the fracture width for a Newtonian fluid of viscosity $\mu$ (Boone and Ingraffea, 1990):

$$q_f = -\frac{\omega^3}{12\mu}\nabla P_f \quad \ldots(8)$$

where $\omega$ is the fracture aperture, $\mu$ is the viscosity of the fracturing fluid, and $\nabla P_f$ is the pressure gradient inside the fracture. The second type is the normal flow which can be determined by taking into consideration the fluid-leak off coefficients. The normal flow can be introduced as follows (Li et al., 2019):

$$q_t = c_t(p_i - p_t) \quad \ldots(9)$$

$$q_b = c_b(p_i - p_b) \quad \ldots(10)$$

where $q_t$ and $q_b$ are the flow rate permeating into surrounding formations; $c_t$ and $c_b$ are the leak-off coefficients for the top and bottom layers of the cracked elements , respectively; $p_t$ and $p_b$ are the pore pressure on the top and bottom surfaces of the cracked elements, respectively; $p_i$ is the pore pressure in the middle of the cracked elements.

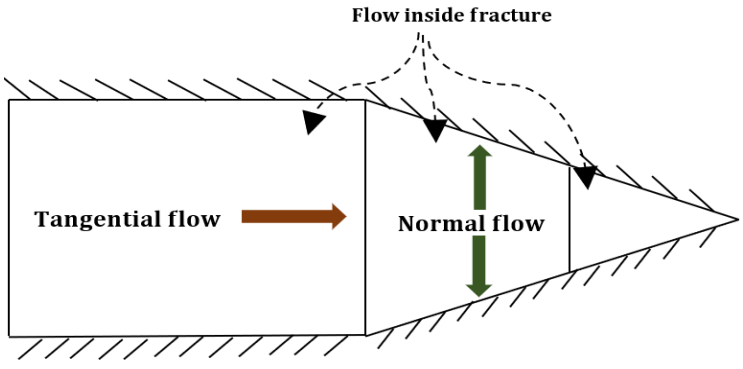


**Figure. 4** Flow of fracturing fluid within the fracture

## 3.5. Model Construction

### *3.5.1. One Stage Hydraulic Fracturing*

Isotropic and vertical transversely isotropic reservoirs undergoing fluid injection are simulated using the coupled pressure/deformation extended finite element method. The size of the model is 300 m along the x- and y- directions (**Figure 5**) . The horizontal wellbore is modeled as a horizontal line in the x-direction and intersects the bottom edge of the reservoir. The cracks intersect the horizontal wellbore and have an initial length of 1 m. All the cracks are open at first to allow the fluid to reach the cracks through the perforated tunnels and the fractures to propagate. The outer boundaries have a zero-displacement boundary condition and constant pore pressure to ensure stability. A concentrated fluid flow is applied through the perforations with different injection rates and times. The reservoir rocks are defined by their porosity, permeability, pore pressure, and elastic properties. The far-field stresses are defined along the x- and y-directions. A fully coupled seepage-stress simulation is performed using the geostatic to model the far-field stresses and a soil analysis steps to simulate fluid injection. The mesh size was chosen to be small enough (0.25 m), to allow the crack to cross an entire element at every simulation time step (Wang, 2015). In all examples, the injection pressure and fracture width are measured at the injection point of the propagating cracks.

The first model is a homogeneous isotropic formation with a single crack intersecting the borehole where we perform fluid injection. The second model is a small scale (lab-scale) isotropic rock, with a circular wellbore intersected by two cracks. These two examples serve as benchmarks to verify the accuracy of the simulations against analytical and experimental results. Then, two fracturing scenarios are

considered. The first scenario includes a single crack undergoing fluid injection to study the effect of the injection rate and the degree of anisotropy on the value of permeability. The second scenario includes three fractures (three clusters) to measure the effect of the cluster spacing on permeability. Moreover, different values of far-field stress are investigated. The model is partitioned to provide an enrichment zone (i.e., zone with fine mesh) at the location of perforations. A mesh sensitivity analysis is performed to obtain the optimum mesh size, and the sweep meshing technique with advancing front is adopted to capture the best fracturing pattern. In all the models, the nodes at the injection point are restricted using the phantom edge nodes to prevent undesirable deformation (Zielonka et al., 2014) (**Figure 6**). **Table 1** lists the duration and injection rate used for all the examples. **Table. 2** and **Table. 3** summarize the fluid and material properties used in the numerical simulations.

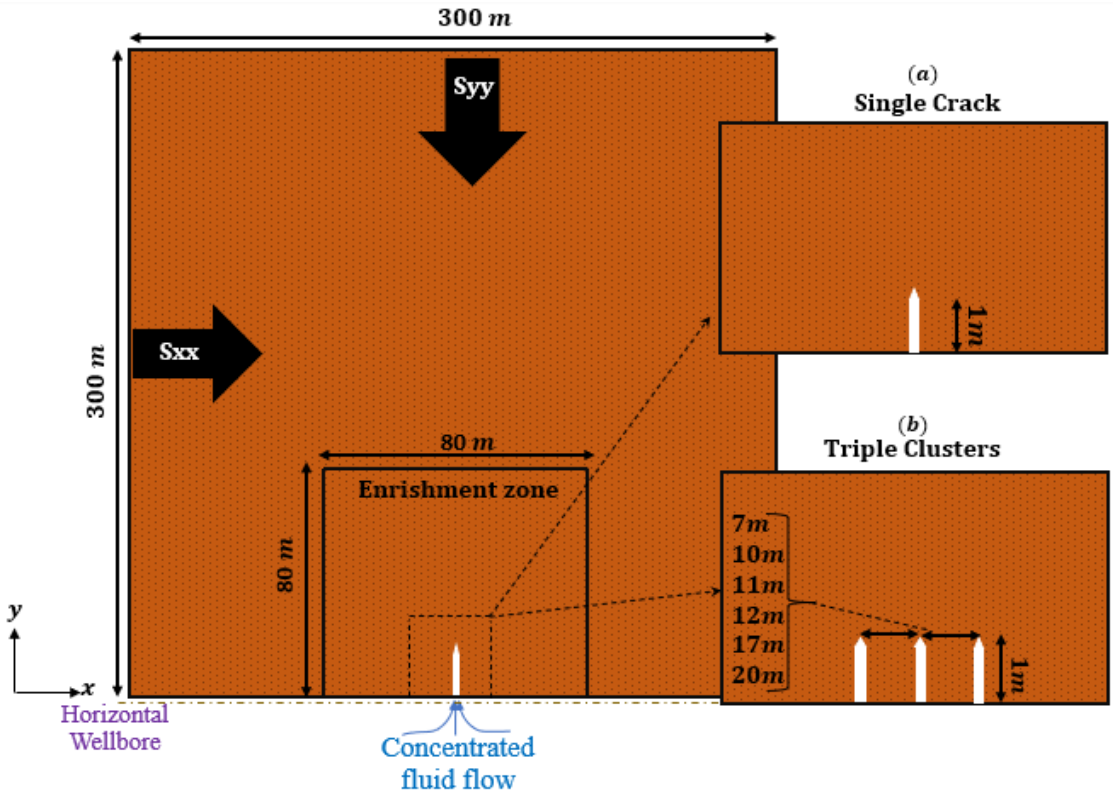


**Figure 5** Model construction for two fracturing scenarios: (a) single crack and (b) triple clusters

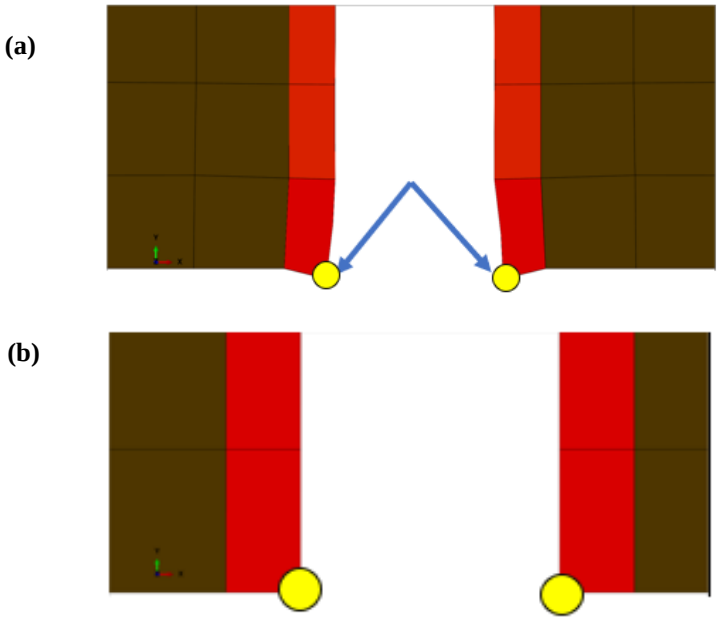


**Figure 6** (a) Undesirable crack aperture at the injection point shown with blue arrows, and (b) correct crack aperture after using the phantom node option at the yellow nodes

**Table 1** Injection times and rates for the numerical models

| Case | Duration (s) | Injection Rate ($m^3/s$) |
|---|---|---|
| KGD | 40 | 1E-3 |
| Experimental test* | - | - |
| Single Fractures | 300 | (1E-5-1E-2) |
| Triple Fractures | 1000 | 1E-4 |

*The values of the injection rate and time equal to the values used in the experimental tests.

**Table. 2** Fluid properties used in the numerical simulations

| Fluid properties | Value |
|---|---|
| Viscosity (cp) | 1 |
| Injection fluid density ($kg/m^3$) | 1000 |

**Table. 3** Input parameters used in the numerical models

| Input Parameters | Value |
|---|---|
| Young's Modulus (GPa) | 15 |
| Poisson's Ratio | 0.25 |
| Tensile Strength (MPa) | 1 |
| Fracture Energy ($J/m^2$) | 100 |
| Matrix permeability (mD) | 1 |
| Matrix porosity | 0.1 |
| $S_{11}$ (MPa) | 25 |
| $S_{22}$ (MPa) | 20 |
| $S_{33}$ (MPa) | 30 |
| Leak-off Coefficient ($m^3$/KPa.S) | 4e-17 |
| Initial reservoir pore pressure (MPa) | 10 |

### *3.5.2. Three Stages Hydraulic Fracturing*

Three multi-stage HFs are developed to study the impact of the cluster spacing and stage spacing in the case of multi-stage injection. To prevent the fractures from closing in the following stages, zero pore pressure boundary conditions are defined after each stage for the created fractures (**Figure 7**), during which the built-up pore pressure in the fractures is allowed to bleed off

into the formation. The zero-pore pressure boundary condition is used to model the presence of proppants in the field. Three fractures per stage are considered with distances of 7 and 12 m between the clusters and 15, 20, 25 m between the stages. **Table 4** lists the duration of multiple fracturing stages and injection rates**. Figure 8**

shows model construction, stages spacing, and cluster spacing used in the multi-stage HF models . The models are performed on ABAQUS 2020 using a High-Performance Computing machine (HPC) with 16 cores per node.

**Table 4** Injection time and rate in each stage

| Case | Duration (s) | Total time (s) | Injection Rate ($m^3/s$) |
|---|---|---|---|
| Initial equilibrium | 1 | 1 | - |
| First-stage fracturing | 400 | 401 | 1E-4 |
| Second-stage fracturing | 400 | 801 | 1E-4 |
| Third-stage fracturing | 400 | 1201 | 1E-4 |

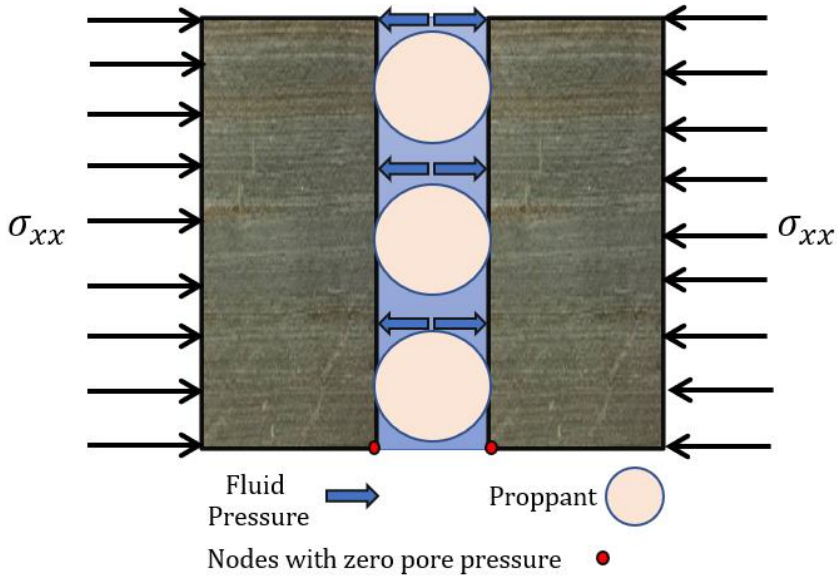


**Figure 7** A schematic of a single crack in the Multistage HF

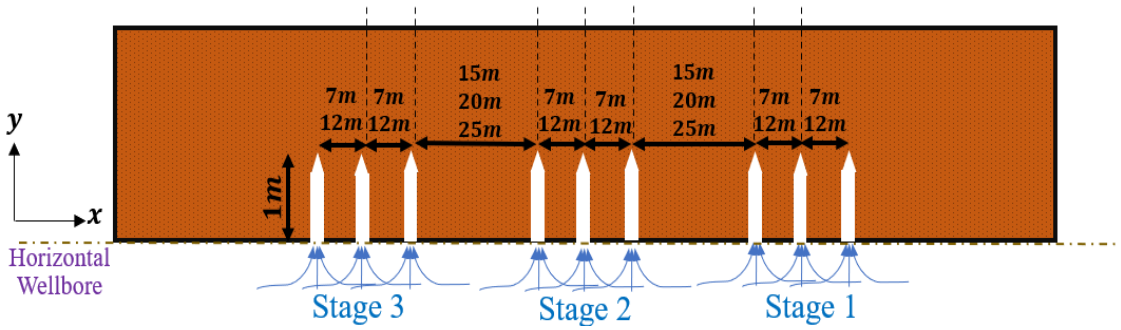


**Figure 8** Model construction for the multistage HF

### *3.5.3. Modified Gueguen and Dienes Method.*

Gueguen.Y and Dienes.J, (1989) developed an analytical model to estimate the permeability of the fractures taking into account the length, width and the distances between the fractures. The fractures are modeled as pipes and the permeability is given by **(Figure 9)**

$$K = \frac{\pi}{32} f \frac{\overline{\lambda r^4}}{\bar{l}^3} \dots (11)$$

where $\bar{\lambda}$ is the length of the pipe, $\bar{r}$ is the radius of the pipe, $\bar{l}$ is the average spacing between the pipes, and $f$ is the fraction of the connected pipes : $0 \leq f \leq 1$.

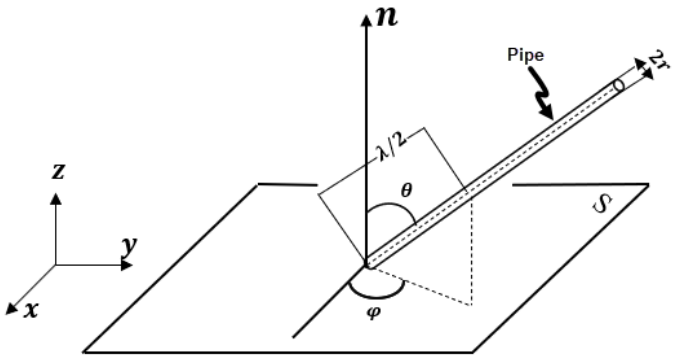


**Figure 9** The pipe model geometry proposed by Gueguen.Y and Dienes.J, (1989)

However, the method proposed by Gueguen.Y and Dienes.J does not consider the presence of proppants within the fractures Therefore, we propose adding a tuning factor $\alpha$ to account for the presence of proppants in the permeability calculation. The factor $\alpha$ is calculated by dividing the permeability of Kozeny-Carman by the permeability obtained from the Cubic Law, $\alpha = \frac{K_{Kozeny-Carman}}{K_{Cubic-Law}}$, where $K_{Cubic-Law} = \frac{h^2}{12}$ (Sarkar, Toksoz and Burns, 2004), and $K_{Kozeny-Carman} = \frac{\emptyset^3}{150(1-\emptyset)^2} D_g$ (Mavko, Mukerji and Dvorkin, 2009), where $h$ is the fracture aperture, $\emptyset$ is the porosity within

the fracture region, and $D_g$ is the diameter of the proppants (assumes sand proppants with a diameter of 2.36 mm).

# CHAPTER 4

# MODEL VALIDATION AND TESTING

## 4.1. Introduction

In order to validate the accuracy of our models, two benchmark examples are performed. A single propagation fracture was simulated first. In this case, the fracture aperture and injection pressure were compared with the KGD analytical solution. After that, we compared our results with a set of laboratory HF operations available in the literature by modeling a lab specimen subjected to the HF operation at different conditions.

## 4.2. KGD Model

The KGD model was developed in 1997 by Khristianovich-Geertsma-de Klerk (KGD). It is used to estimate the fracture width, length, and injection pressure for HF applications. The fracture cross-section is assumed rectangular with a constant width along the fracture height (**Figure. 10**). The model assumes a linear isotropic elastic formation, a plane strain fracturing deformation in a horizontal plane and a laminar flow. The model neglects fracture toughness. The fracture width ($w_0$), length ($L$), and injection pressure ($P_w$) are given by (Nasiri, 2017;Yao et al., 2015)

$$L = 0.48 \left(\frac{8GQ^3}{(1-\nu)\mu}\right)^{\frac{1}{6}} . t^{\frac{2}{3}} \quad \ldots(12)$$

$$w_0 = 1.32 \left(\frac{8(1-\nu)Q^3\mu}{G}\right)^{\frac{1}{6}} . \mathrm{t}^{\frac{1}{3}} \quad \ldots(13)$$

$$P_w = \sigma_{min} + 0.96 \left(\frac{2G^3 Q\,\mu}{(1-\nu)^3 L^2}\right)^{\frac{1}{4}} \quad \ldots(14)$$

where $G$ is the shear modulus, $\mu$ is the fluid viscosity, $\nu$ is Poisson ratio, $t$ is the injection time, $Q$ is the injection rate, and $\sigma_{min}$ is the minimum horizonal stress. The injection pressures and fracture aperture obtained for a single crack using ABAQUS 2020 are compared with the analytical solution (the KGD model).

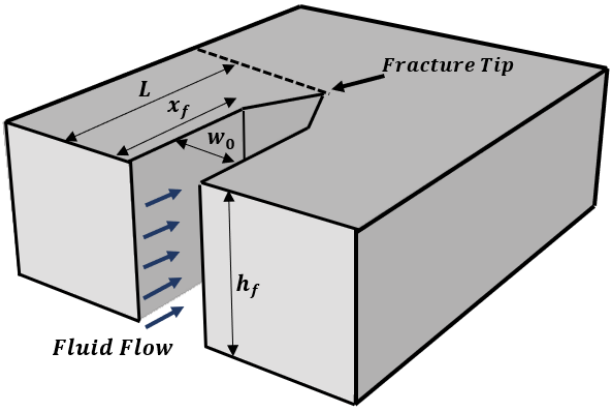


**Figure. 10** Geometry of the KGD model,

**Figure. 11** show a good agreement between the numerical models and the analytical solution for a single crack subject to a specific injection rate. The relative error between the maximum injection pressure magnitude is 5%, while the error between the aperture obtained numerically and analytically is 3%.

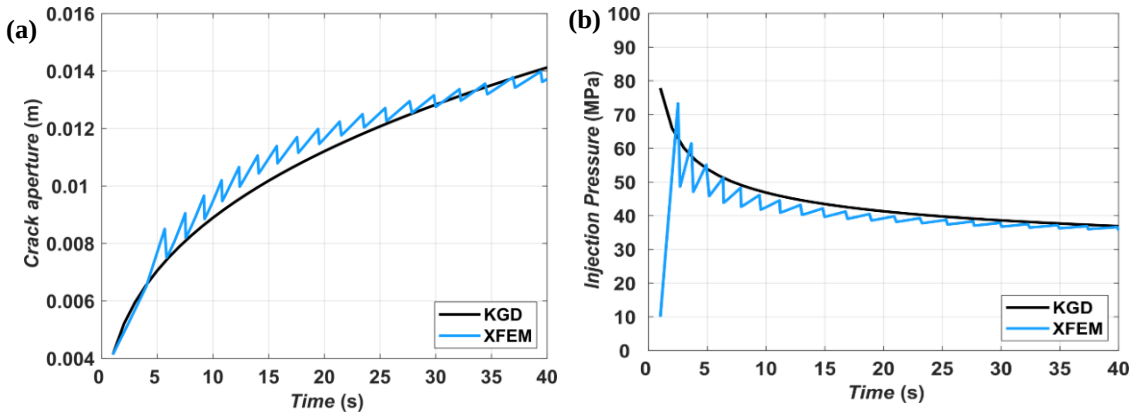


**Figure. 11** Comparison of the (a) crack aperture and (b) injection pressure obtained using the XFEM and KGD analytical solution

### 4.3. Verification against Laboratory Tests

To model HF in the lab, a cube-shaped rock is drilled at the center to model a borehole. A tube is inserted in the hole and perforations intersect the borehole and the tube. A fluid is injected through the tube at a given injection rate which allows the fractures to initiate and propagate. We compare the results obtained using the XFEM to laboratory experiments conducted by Cheng and Zhang's (2020). They used 300 × 300 × 300 mm granite at high temperatures. The minimum, maximum, and overburden principal stresses are 4, 12, and 8 MPa, respectively. Water with 1 cp viscosity is injected in the borehole that has an internal pressure of 55.3 MPa. We also compare the results of the XFEM to the study conducted by Zhao et al., (2016) where they apply the HF test to a concrete specimen of 300 × 300 × 300 mm. In their work, they investigate the effect of the bedding plane thickness on the breakdown pressure of concrete, using water as their injection fluid. The minimum, maximum, and overburden principal stresses are 1, 2.1, and 2.9 MPa, respectively. Finally, we compare our results to the work of M. Chen et al., (2010) who studied the impact of the oriented perforation on the breakdown pressure. The fluid viscosity used is 133 cp to reduce the influence of toughness and to compensate for the low injection rate used in laboratory models. The minimum, maximum, and overburden principal stresses are 1, 4.15, and 2.9 MPa, respectively and the sample dimensions are 300 x 300 x 300 mm. In all the experimental studies, no initial pore pressure was present within the block sample. **Figure 12** shows the geometry of the benchmark example and **Figure 13** compares the crack path obtained in the experimental tests and the numerical models. **Table 5** summarizes the breakdown pressure obtained in the experimental tests and numerical models.

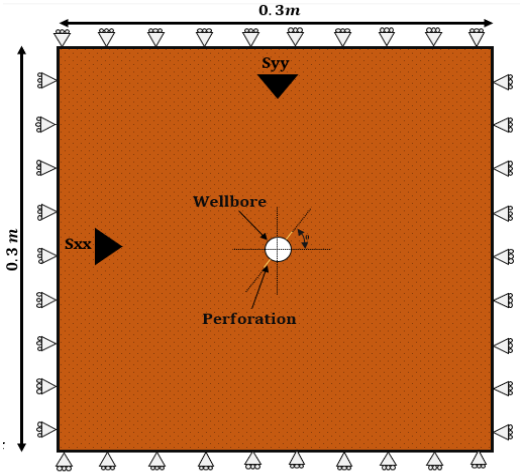


**Figure 12** The geometry of the benchmark example. The circle illustrates the wellbore.

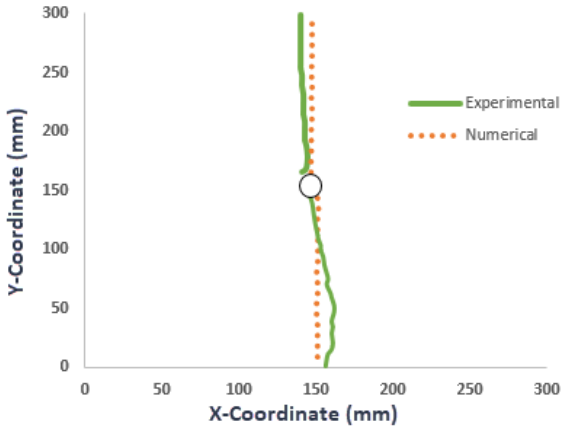


**Figure 13** Comparison between the crack paths obtained in the experimental test of Cheng and Zhang, (2020) and the numerical results. The initial perforation angle is at 90 degrees (vertical). The crack paths obtained experimentally is reproduced using the Plot Digitizer tool from Figure 14 in Cheng and Zhang, (2020)

**Table 5** Comparison between the experimental tests and numerical models

| | (Cheng and Zhang 2020) | (Zhao et al. 2016) | (M. Chen et al., 2010) |
|---|---|---|---|
| Measured Breakdown Pressure (MPa) | 36 | 8.01 | 6.5 |
| Estimated Breakdown using the XFEM (MPa) | 33 | 7.56 | 7 |

# CHAPTER 5

# RESULTS AND ANALYSIS

## 5.1. Introduction

This chapter presents the results of the HF operation using the XFEM under the influence of different injection rates, mechanical contrast between the layers, cluster spacing, and multi-stage HF. In the study of cluster spacing, we consider three different scenarios. In the first and second scenarios, the horizontal far-field stress is greater and smaller than the vertical far-field stress. A VTI medium with an MC value equal to 6 is considered in the third scenario. Moreover, we measure the permeability using the method of Gueguen and Dienes.

## 5.2. Single Crack (Isotropic and VTI Formations)

### *5.2.1. The Influence of the Injection Rate*

Increasing the injection rate by a factor of 10, 100, and 1000 has a significant impact on the fracture geometry and breakdown pressure. **Figure 14** shows the final evolution of the injection pressure and crack aperture for an injection rate of 1E-3 $m^3/s$ and after 300 s of injection. The injection pressure ramps up linearly in the first 10 s, allowing the fluid to flow gradually. The maximum crack aperture and length obtained at the end of the injection are 0.022 $m$ and 22 $m$, respectively, while the breakdown pressure is obtained earlier after 10 s and equals 69.2 MPa. Higher injection rates result in wider and longer cracks **(Figure 15 a)**. Increasing the injection rate causes the injection pressure to increase (**Figure 15 b**). This occurs because higher injection rates result in more fluid remaining in the cracks, leading to wider and longer

cracks (Haddad and Sepehrnoori, 2016; Wang et al., 2016). Therefore, the fluid does not have enough time to infiltrate into the formation and the rock will fail at a relatively high breakdown pressure (Zhuang et al., 2019). The effect of the injection rates on a VTI formation is also analyzed. The degree of anisotropy is 6 i.e., $E_V/E_H = 6$, where $V$ denotes vertical and $H$ denotes horizontal. A more detailed analysis of the effect of the degree of anisotropy is given in the next section. **Figure 16 a** shows that a non-planar propagation is obtained for an injection rate of 1E-3 $m^3/s$. The crack will tend to kink away from the harder material toward the soft material. In such situations, high compression stress on the proppants may occur and this might result in the proppant being compressed, crushed, and flowed out, leading to a reduction in the crack width (Maslowski, Kasza and Wilk, 2018). However, a fracture induced at smaller rates (e.g., 1E-4 and 1E-5 $m^3/s$) has a more planar trajectory as the applied fluid allows the cracks to propagate less in length and not to propagate further (**Figure 16 b** and **c)**. Conversely, injection at a relatively high rate (i.e., 1E-2 $m^3/s$) allows the crack to penetrate the weak material showing higher length, width, and greater injection pressure . In this case, the crack also shows a planar propagation. **Figure 17** shows the crack aperture, and the injection pressure as a function of time for an injection rate of 1E-3 $m^3/s$. A decrease in the aperture and injection pressure is observed after 90 s, which is after the crack deviates. The results of the crack aperture, length and injection pressure for the VTI formation are depicted in **Figure 18**.

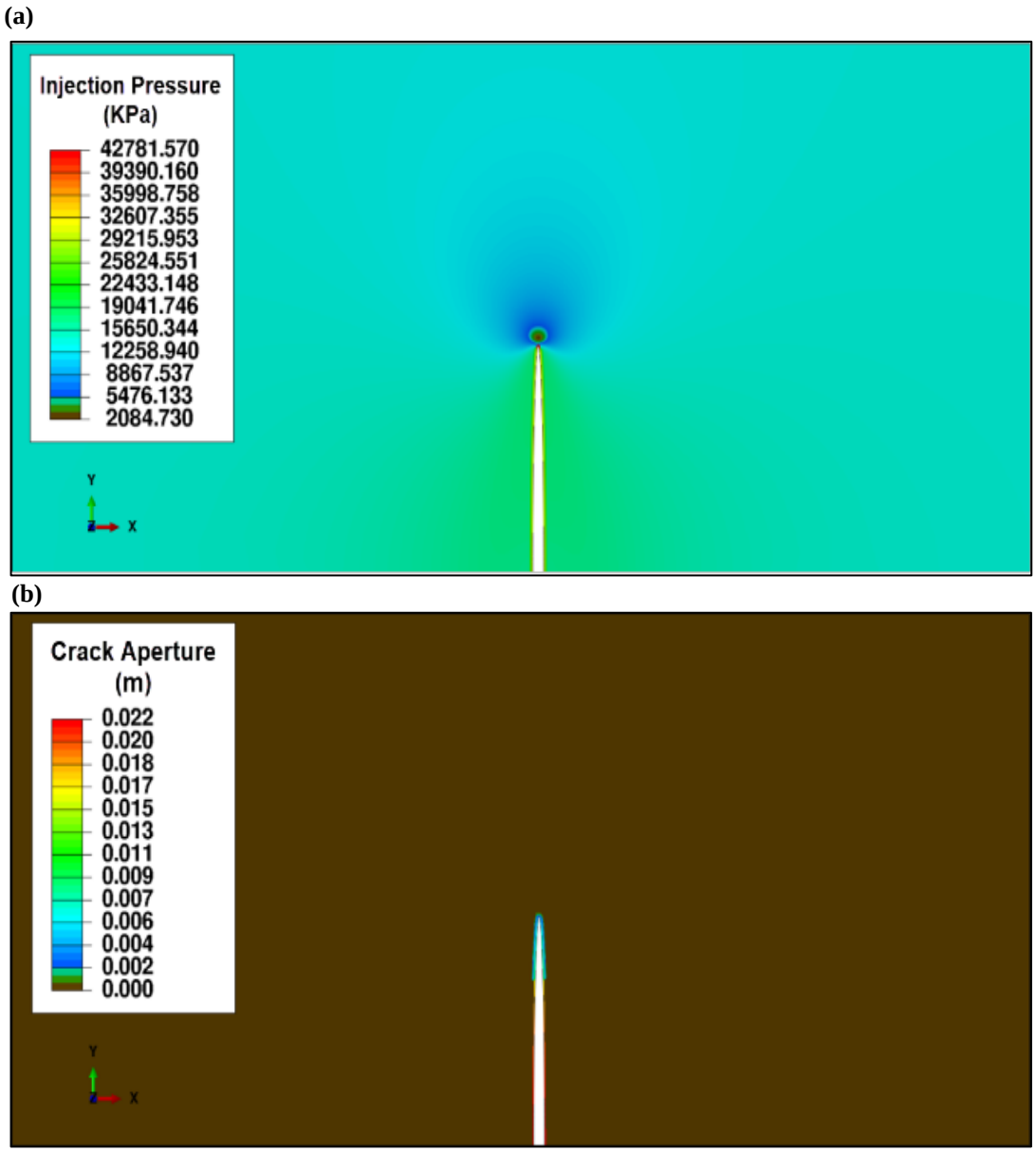


**Figure 14** The final of evolution of (a) injection pressure and (b) crack aperture after 300 s of injection. The injection rate is 1E-3 $m^3$/s. The displacement is magnified 70 times for better crack visualization

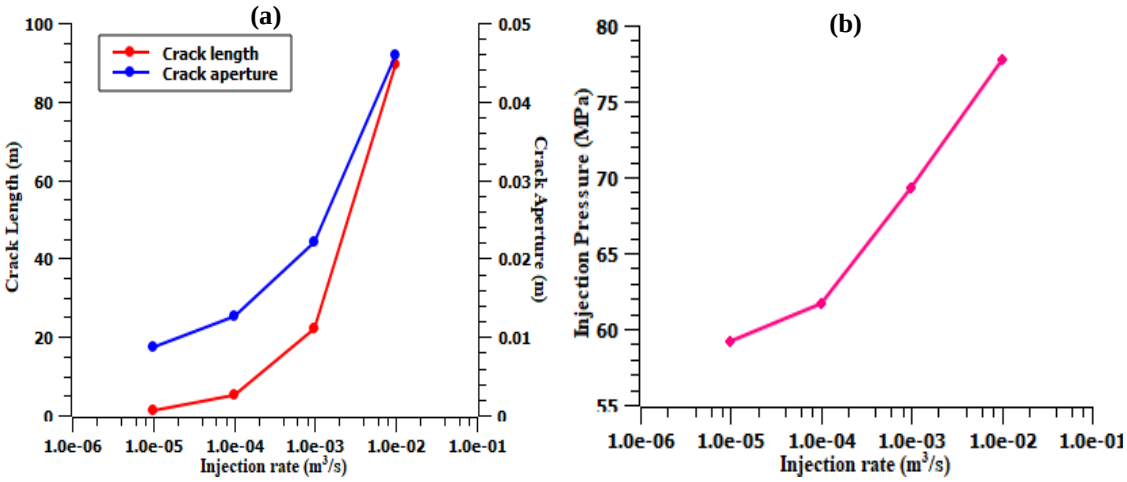


**Figure 15** Comparison of (a) crack aperture, (b) length, and (c) crack injection at different injection rates for a single crack obtained after 300 s of injection

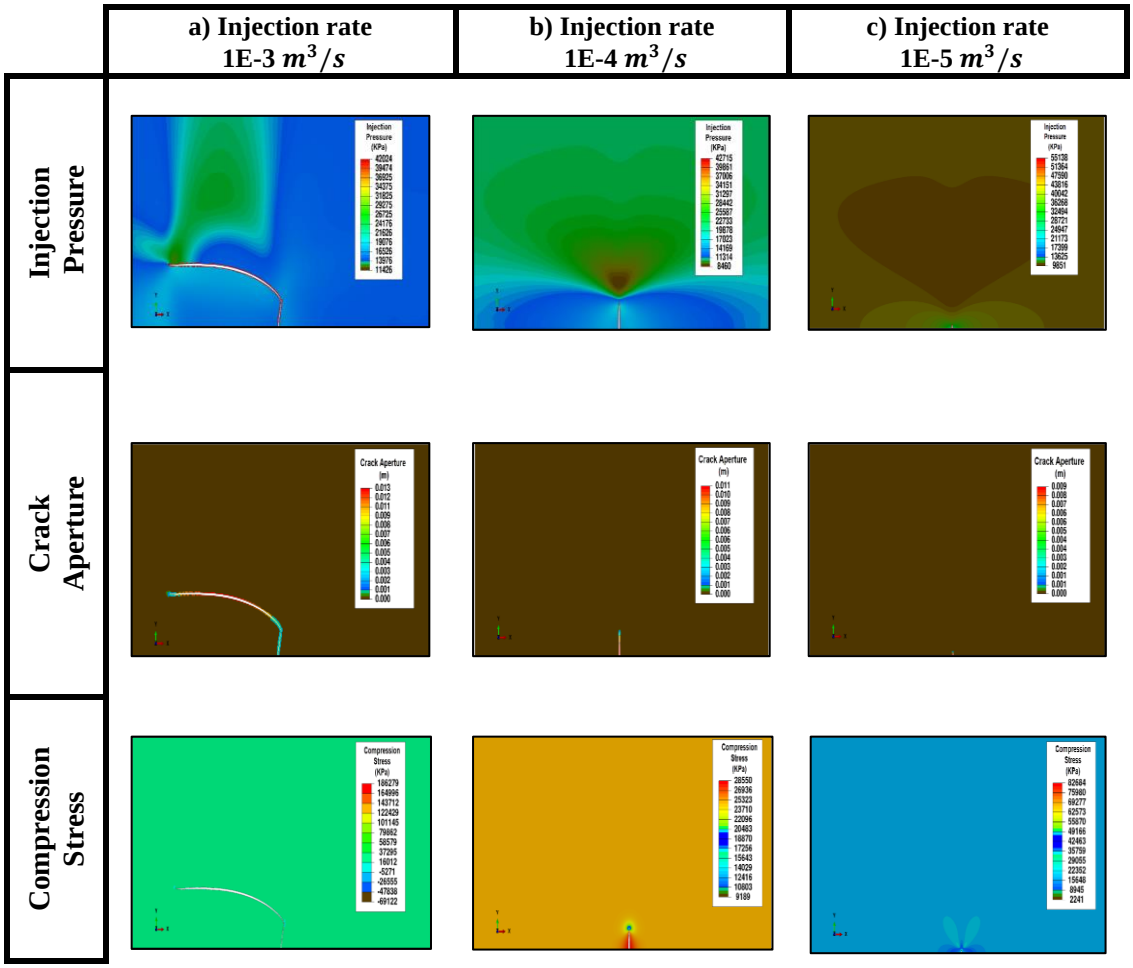


**Figure 16** Injection pressure, crack aperture and compression stress observed at different injection rates for a single crack in a VTI formation. For better crack visualization, the displacement is magnified 70 times

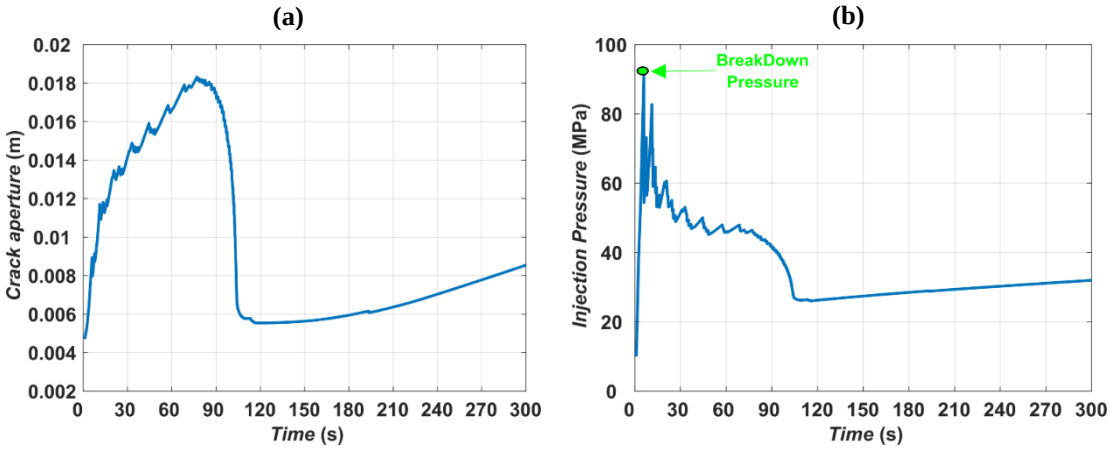


**Figure 17** (a) Crack aperture, and (b) injection pressure as a function of time for the VTI case. The injection rate is 1E-3 $m^3/s$

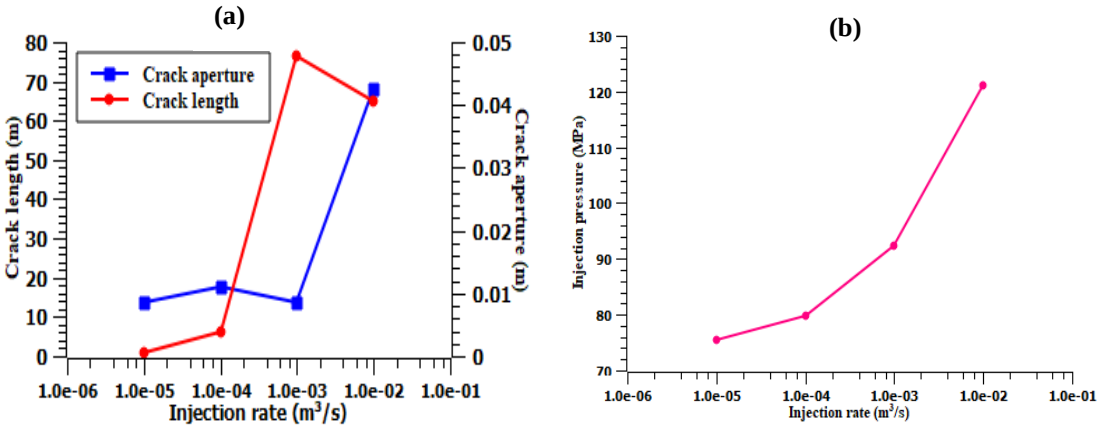


**Figure 18** Comparison of the (a) crack aperture, length, and (b) injection pressure at different injection rates for a single crack obtained at the end of injection

### *5.2.2. The Influence of the Mechanical Contrast*

The HF model is applied to VTI formations with four different mechanical contrast (MC) or degree of anisotropy. **Figure 19** shows the crack aperture and injection pressure observed for MC = 4, 5, and 6. A high degree of anisotropy is found in liquid-rich unconventional shales such as the Nordegg Member in Alberta, Canada (Cui, Glover and Wust, 2014). As the MC increases, the fracture does not propagate in the direction of the maximum horizontal stress but deviates towards the weak bedding planes (**Figure 19 a** and **b**). These observations are consistent with experimental work that showed that the extent of fracture reorientation increases as the contrast in Young's modulus increases (AlTammar, Agrawal and Sharma, 2019). When the MC decreases, the fracture propagates vertically. A small deviation is observed when $E_V/E_H = 4$ (**Figure 19 c**) and the propagation is vertical when $E_V/E_H = 1.5$. **Figure 20** shows that the crack aperture decreases when the MC contrast increases (**Figure 20 a**), whereas the length and injection pressure increase as the value of MC increases (**Figure 20 a** and **b**), respectively.

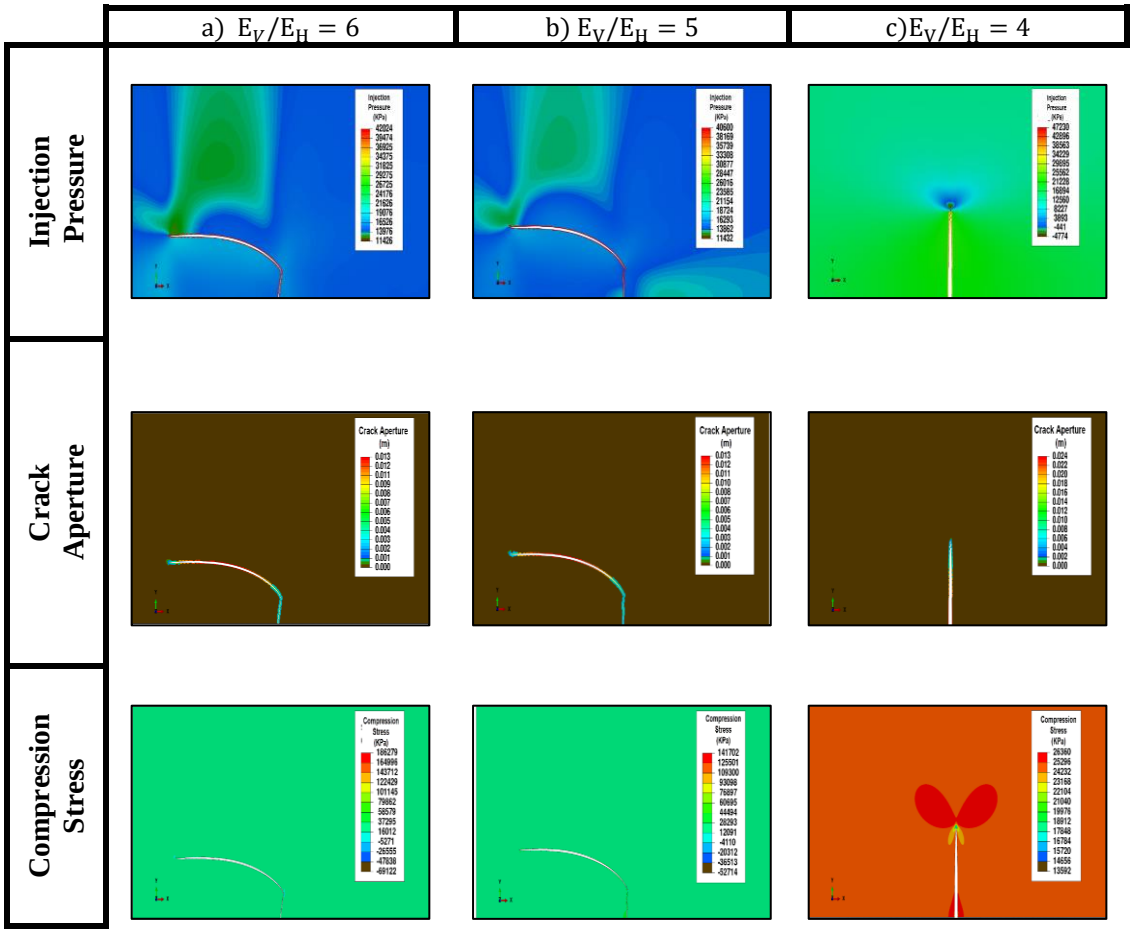


**Figure 19** Injection pressure, crack aperture and compression stress at different MC obtained for a single crack at the end of injection. For the better crack visualization, the displacement is magnified 70 times

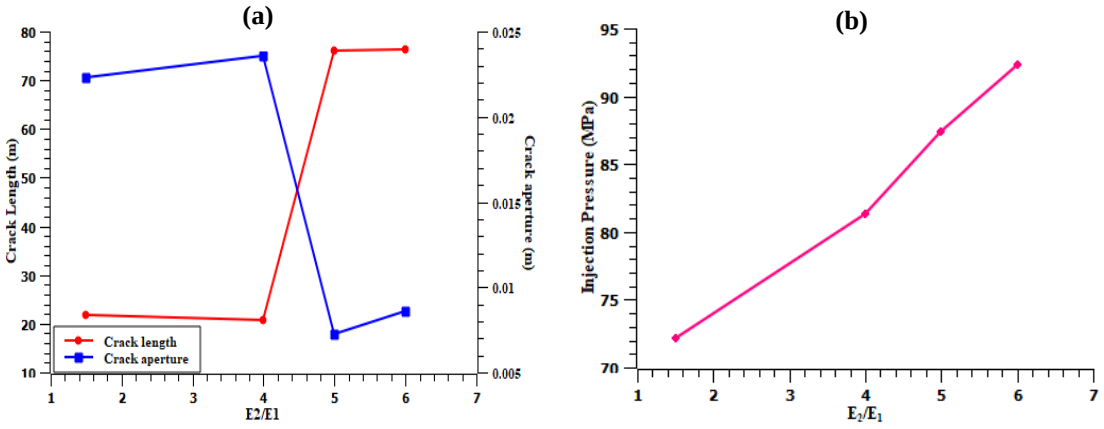


**Figure 20** Comparison of (a) crack aperture, length, and (b) injection pressure at different MC for a single crack after 300 s of injection

## 5.3. Triple Clusters (One Stage)

### *5.3.1. The Influence of Cluster Spacing*

5.3.1.1. Crack Geometries and Injection Pressure

Cluster spacing is considered key to maximizing initial gas production and is needed to identify the fractured area and hence the distance between wells (Yu and Sepehrnoori, 2013).

**Figure 21** displays the final progression of crack opening, injection pressure, and compression stress observed after 1000 s of the injection when the distance between the clusters is 7 m and when $S_{xx} > S_{yy}$, $S_{yy} > S_{xx}$, and MC=6**.** When $S_{xx} > S_{yy}$, the side cracks will propagate away from the middle crack when the injection pressure increases. As the fractures deviate, their width decreases, which increases the pressure around the middle crack (see the blue circle in the stress map in **Figure 21 a**. The area with high stress prevents the middle crack from propagating further vertically and leads to a wider fracture aperture (Haddad and Sepehrnoori, 2016). A different crack pattern is observed when the overburden stress is greater than horizontal stress ($S_{yy} > S_{xx}$). The middle crack has a larger length and a smaller aperture. In this case, the side cracks grow toward the top boundaries, and the crack apertures are wider **Figure 21 b**. When the MC = 6, the side and middle cracks deflect toward the edges, showing a nonplanar propagation **Figure 21 c**. The presence of the high mechanical contrast, in this case, results in additional extensional stress on the fractures experienced by the strongest layer (Douma et al., 2019). Reducing the MC, however, allows the cracks to propagate similarly to the case of isotropic formation. Moreover, the effect of the tensile stresses and the contrast between the far-field stresses on crack propagation will dominate when the contrast between the elastic moduli decreases. Similar observations are obtained

when increasing the distance between clusters from 7 m to 11 m. Moreover, the side cracks require a longer time to close when the distance between clusters increases if $S_{xx} > S_{yy}$.

When the distance between the clusters is 12 m the results show that the side and middle cracks extend vertically, showing the beginning of a planar growth. The cracks expand further vertically when $S_{yy} > S_{xx}$ (**Figure 22 b)**. The fractures grow independently as the space between clusters increases, and the path is similar to that of a single crack case. This occurs because the influence of fractures on each other decreases as the distance between them increases. No deflection is observed when the distance between clusters is 20 m as the side and middle cracks have a planar propagation when $S_{xx} > S_{yy}$ and $S_{xx} < S_{yy}$ **(Figure 23 a** and **b**). However, owing to the strong anisotropy reflected by the high MCs in the VTI model, fractures tend to develop towards the weak material and have a smaller width compared to the cases when $S_{xx} > S_{yy}$ and when $S_{xx} < S_{yy}$ at a distance of 20 m (**Figure 23 c**).

**Figure 24** shows the aperture of the left, right, and middle cracks recorded at the injection point for the various conditions indicated previously. When the distance between the clusters is 7 m, the results reveal that the apertures of the left and right cracks are minimal for $S_{xx} > S_{yy}$, and they are close to the apertures in the VTI model for MC = 6. Moreover, the aperture of the right crack in this case shows a smaller value in comparison with the left crack. This can be interpreted by the large deflection of the middle crack to the right which causes the right crack to propagate further in length and less in aperture (**Figure 21**). However, when $S_{yy} > S_{xx}$ and the MCs are small (e.g., 1.5 and 4), the results illustrate that the aperture of the left and right cracks is maximal.

The aperture of the middle crack shows an opposed behavior, as it would be largest when $S_{xx} > S_{yy}$ and high MCs. and minimal when $S_{yy} > S_{xx}$, in addition to the conditions where the MCs are small (ex. 1.5 and 4). The aperture of the right, left and middle cracks start to stabilize when the distance between the clusters equals to 12 m (the beginning of the planar growth) Increasing the distance between clusters to 20 m causes the cracks to have equal apertures at the end of injection, It is also observed that the maximum injection pressure is recorded when $S_{xx} > S_{yy}$ and for high MCs, whereas the minimum injection pressure is obtained for formations with low MCs (

**Figure 25**). Increasing the distance between the clusters, however, causes the injection pressure to decrease. The results are in line with the configurations of side and middle cracks as the compression region in front of the shorter cracks, when the distance is small, prevents them from propagating further, which significantly impacts the injection pressure and crack aperture.

5.3.1.2. Permeability Estimation

**Figure. 26** shows the results of permeability for the left, right, and middle cracks. In all cases, increasing the distance between the clusters induces a decline in permeability as the crack geometries tend to have the same values by decreasing cluster spacing. At a distance of 7 m, the left and right cracks have the smallest permeability. This phenomenon can be explained by the large deviation observed that induced crack closure after 1000 s of injection. The deviation of the middle crack towards the right affects the value of the aperture, length, and the resulting permeability of the right crack more than the left crack. When $S_{xx} > S_{yy}$ and when MC = 1.5 and 4, the permeability shows the highest value due to the vertical growth without any significant apparent deflection observed during the injection (planar propagation). The permeability of the

middle crack, on the other hand, is small and has the same value for all cases where the distance between the clusters is 20 m, and is maximal when the distance between the clusters is 7 m, $S_{xx} > S_{yy}$ and MC=6 and 4.

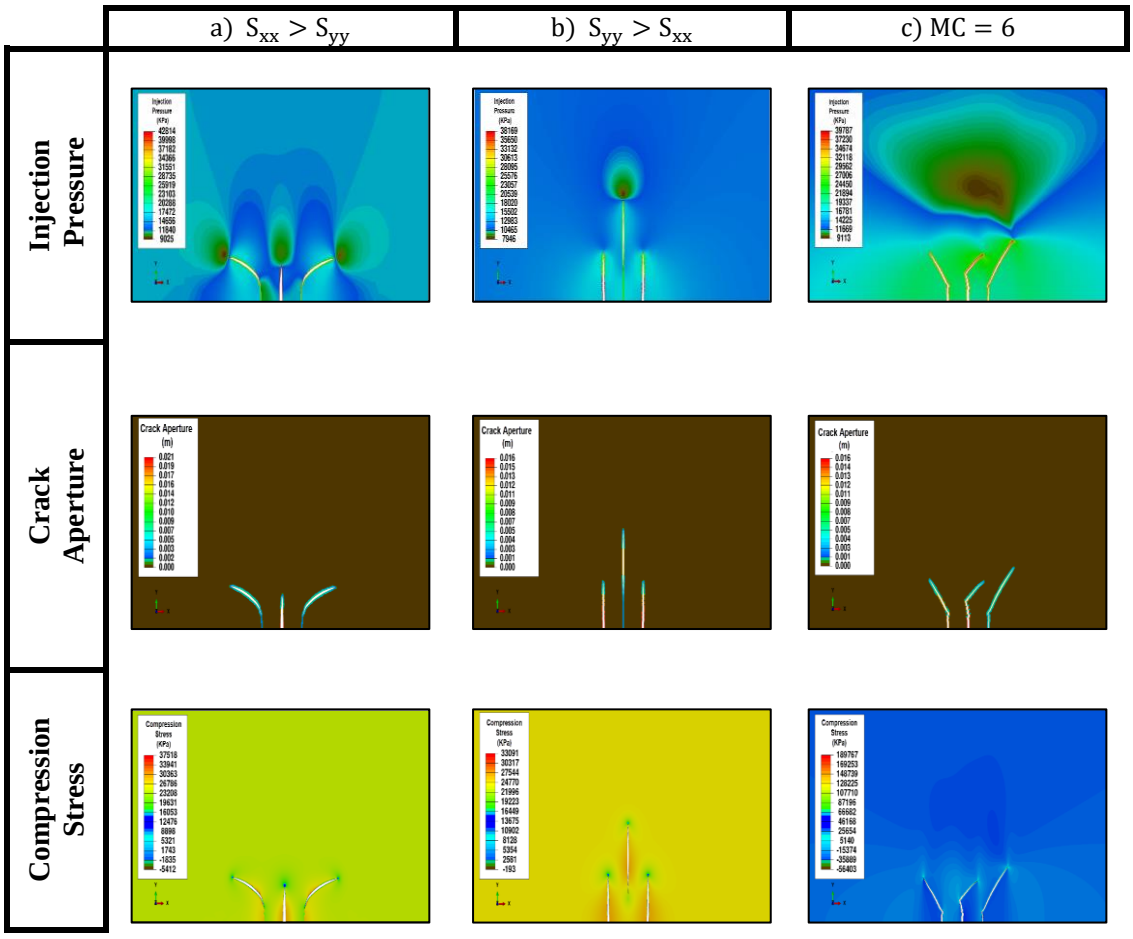


**Figure 21** Injection pressure, crack aperture and compression stress when the distance between the clusters is 7 m. For the better crack visualization, the displacement is magnified 70 times

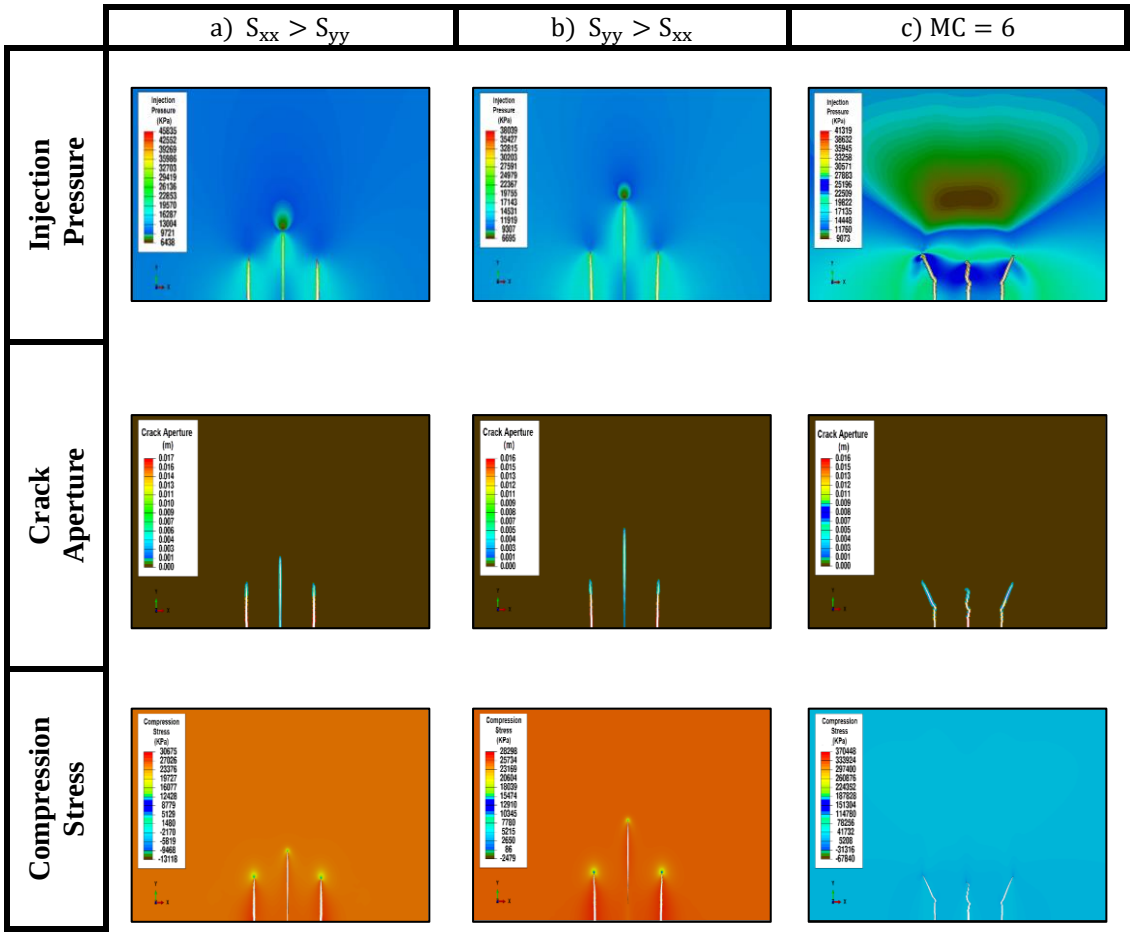


**Figure 22** Injection pressure, crack aperture and compression stress observed when the distance between the clusters is 12 m. For the better crack visualization, the displacement is magnified 70 times

.

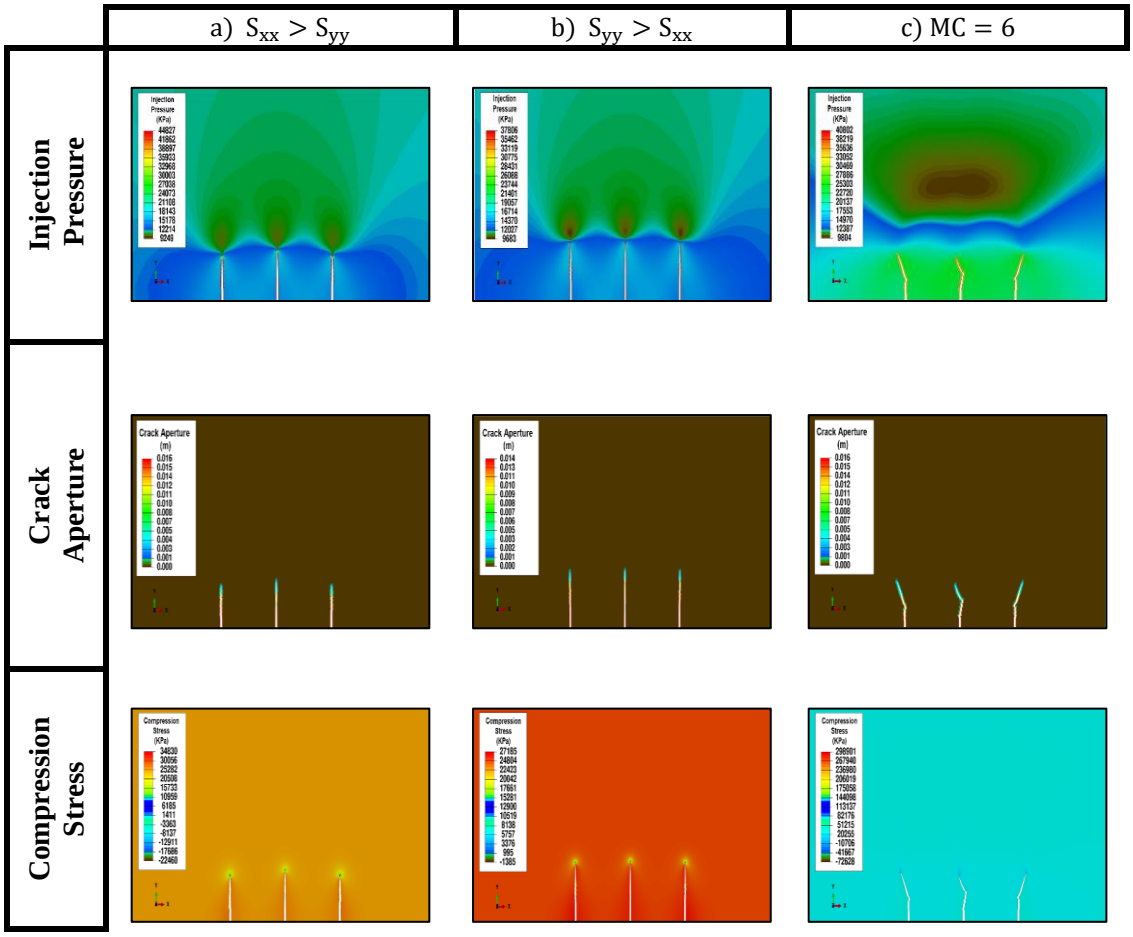


**Figure 23** Injection pressure, crack aperture and compression stress observed when the distance between the clusters is 20 m. For the better crack visualization, the displacement is magnified 70 times

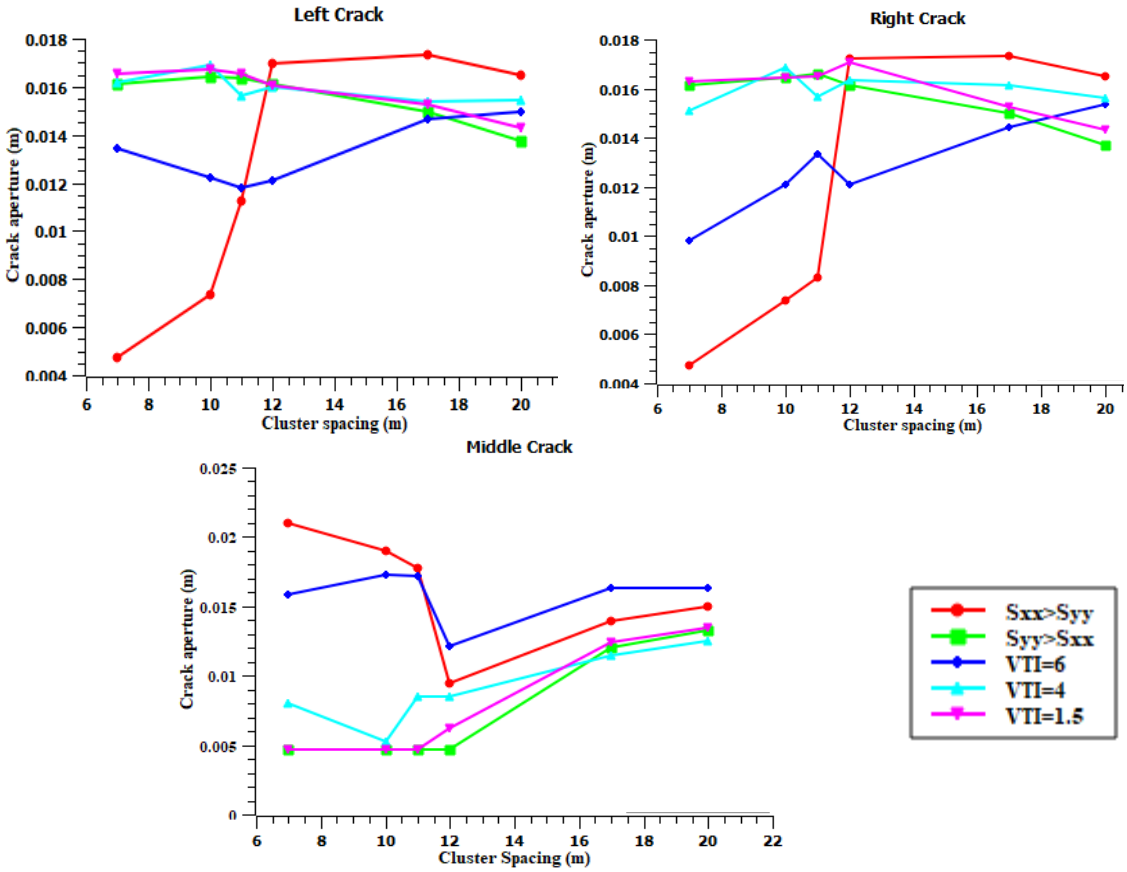


**Figure 24** Crack aperture recorded at the injection point for different spacing between the clusters

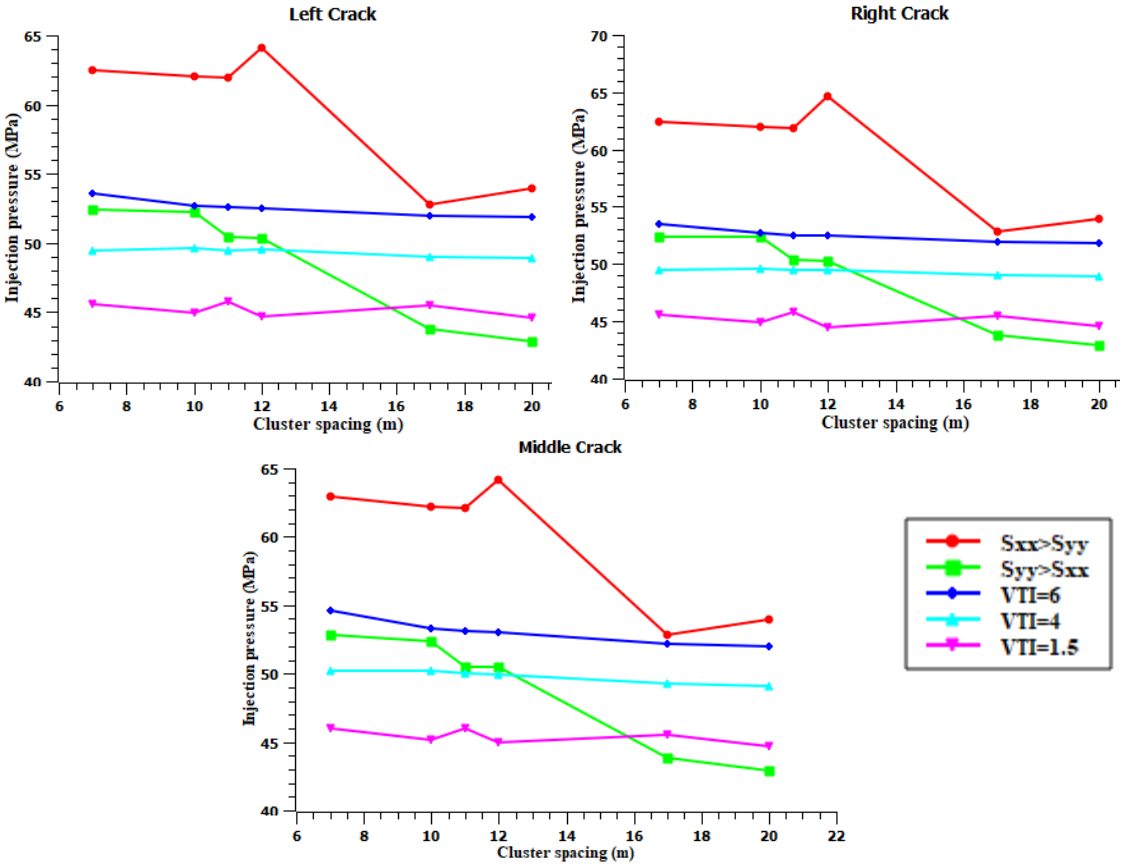


**Figure 25** Injection pressure recorded at the injection point for different spaces between the clusters

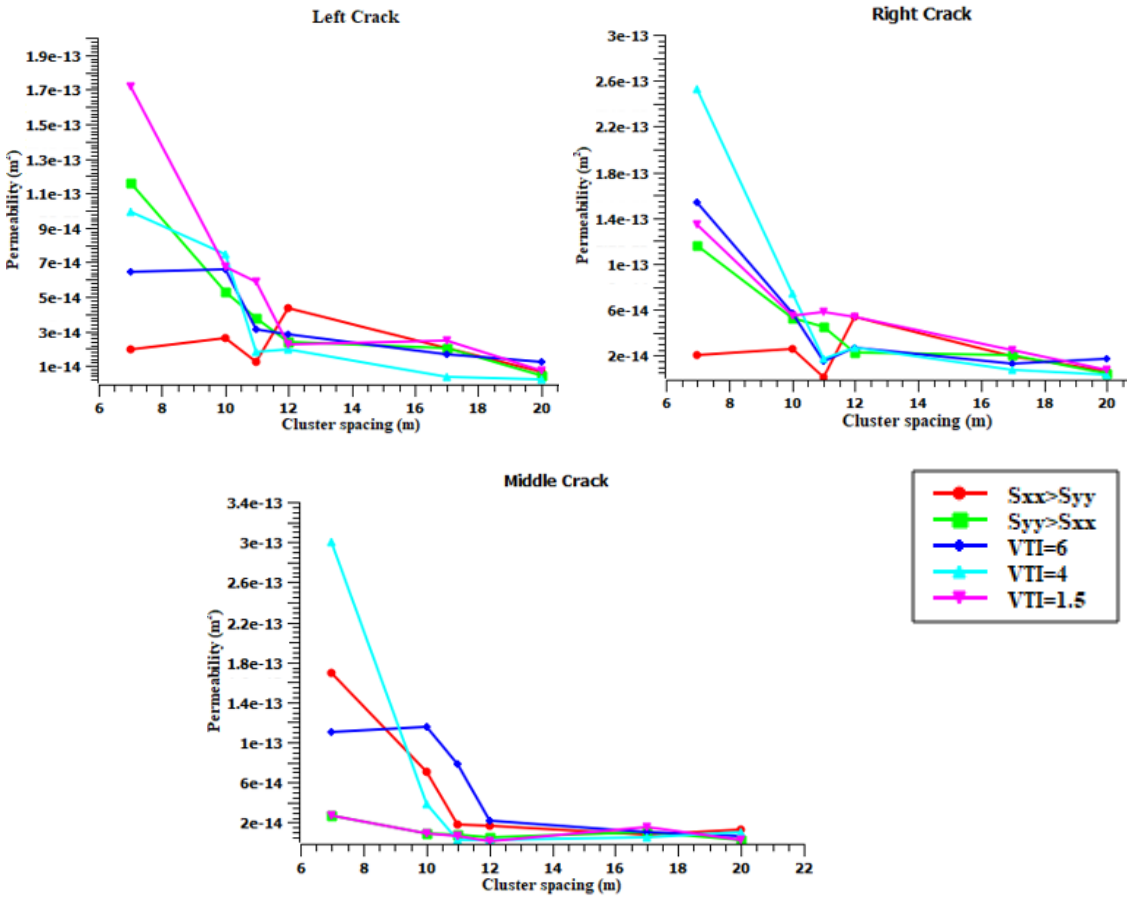


**Figure. 26** Permeability estimation using the modified Gueguen and Dienes method,

### 5.4. Triple Clusters (Three Stages)

**Figure 27** displays the final fracture evolution for the multistage HF when the distance between the clusters is 12 m and between the stages is 20 m. The fractures propagate along the original perforations, with no clear deflection at the end of injection in each stage (planar propagation). The results agree with the models shown in **Figure 22** where the beginning of the planar growth is observed when the distance between the clusters is larger than 12 m. The high compression stress observed near the fractures in the first and second stages (the red region in the stress surface map) is due to the zero pore pressure nodes that will be activated at the end of each stage. This can be justified by the presence of proppants that will allow the crack to remain open, prevent any further propagation crack apertures reduction.

**Figure 28** shows that when the initial perforation cluster space is 7 m and the distance between the stages is 20 m, the apertures of the middle cracks at all stages are smaller than the apertures of the side cracks. The middle crack, however, in the first stage expands more in length than the middle crack in the following stages, showing a high reduction in its aperture at the end of the first stage, which is compatible with what we observed in **Figure 21**.

The fracture zone area is calculated by adding the product of the width by the length of fractures for all the fractures. **Figure 29** summarizes the final fracturing area obtained at the end of the three stages and when the distances between clusters are 7 and 12 m and the distances between stages are 15, 20, and 25 m. The results reveal that in the multistage HF, tight clusters increase the fracturing area. The injection pressure for each fracture is then calculated along the horizontal wellbore. It is almost equal for all the fractures, which can be considered equal to the wellbore pressure. **Figure 30** shows

the average injection pressure of the wellbore recorded at the end of the final stage. When the distance between clusters is 7 m the injection pressure is lower than that when the distance is 12 m. This appears to be consistent with the research conducted by Basin, Study and Wells, (2017), that showed that tighter fracture spacing leads to a higher production rate, faster depletion, and higher recovery efficiency.

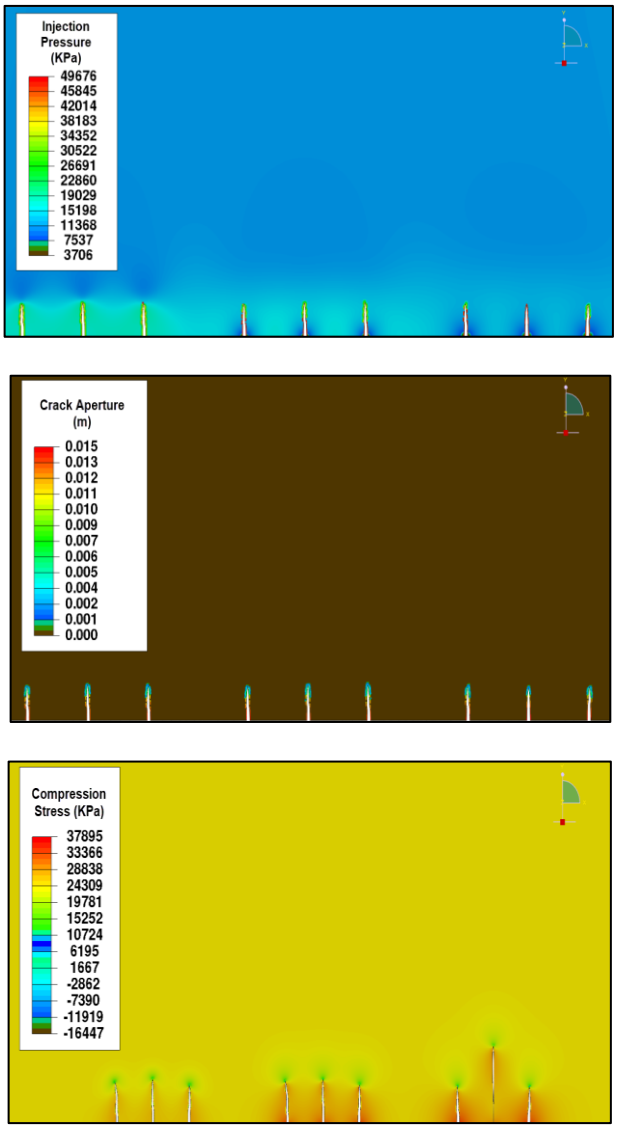


**Figure 27** The final fracture evolution in the multistage HF when the distances between the clusters and stages are 7 and 20 m, respectively

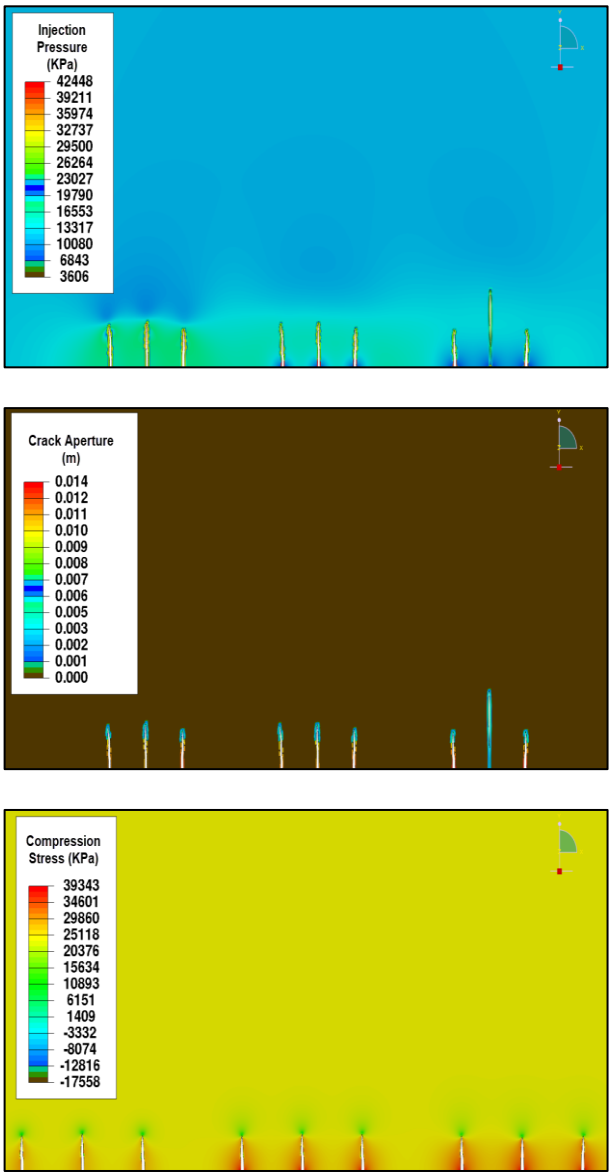


**Figure 28** The final fracture evolution in the multistage HF when the distances between the clusters and stages are 7 and 20 m, respectively

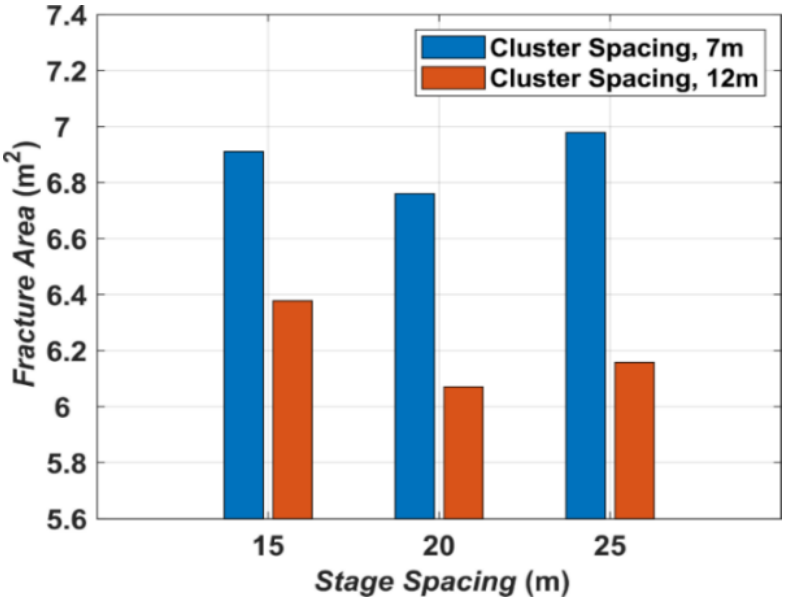


**Figure 29** The final fracture area recorded at the end of the third stage when the distances between the clusters are 7 and 12 m

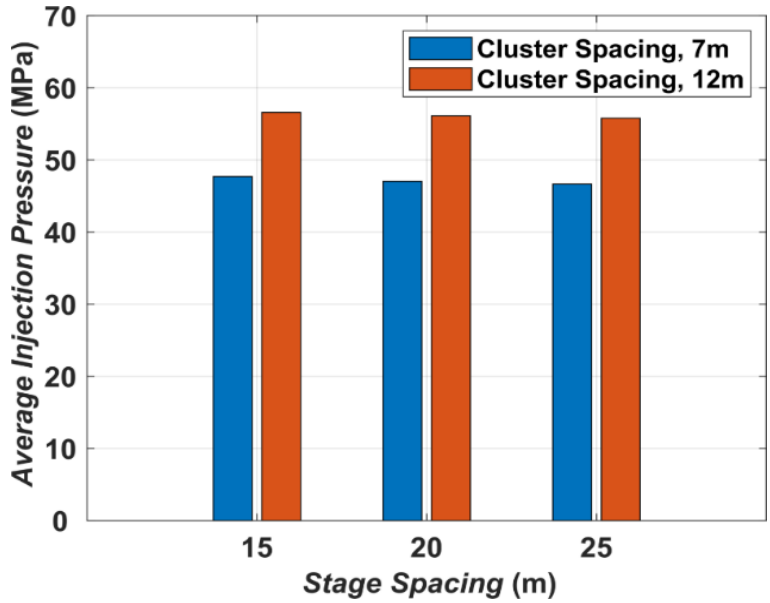


**Figure 30** The average injection pressure recorded at the end of the third stage when the distances between the clusters are 7 and 12 m

# CHAPTER 6

# CONCLUSION AND DISSCUSION

## 6.1. Introduction

This chapter aims to discuss the relevance of the results obtained in the previous chapter and relate them to the HF operation in the field and the laboratory. Conclusion summarizing all the results obtained have been drawn. Future work is suggested at the end in order to improve the models and make them more realistic and effective.

## 6.2. Discussion

Our study shows that the MC between the layers, the distance between the clusters and stages, stress distribution, their magnitudes, and the choice of an injection strategy (i.e., injection rates) are important factors in determining the cracks growth and propagation, and hence optimizing the permeability of the fractured region. According to our results, the direction of propagation depends on both the injection rate and the MC value simultaneously (**Figure 31)**. Fractures tend to deflect toward the weak material when the ratio between the elastic modulus is larger than 4 (i.e. $E_V/E_H = 4$) and when the injection rate is between 1E-4 and 1E-3 $m^3/s$ (**Figure 31 a**). In these cases, even under the impact of far-field stresses, it is easier for the fracture to initiate and propagate parallel to the weak planes instead of growing towards the interfaces (AlTammar, Agrawal and Sharma, 2019). Applying a higher injection rate, however, while maintaining the same conditions allows the fractures to propagate through the interface into stronger layers (**Figure 31 b**). This seems reasonable as the induced stress caused by the high injection rate will be higher than the concentrated stress in the weak

planes which are mainly compressive stresses. However, the value of the injection rate must be chosen carefully. The HF operations at high injection rates may trigger seismicity at different magnitudes because it can cause an increase in the fluid pressure in the fault zones (if fractures are connected to faults) (Davies et al., 2013).

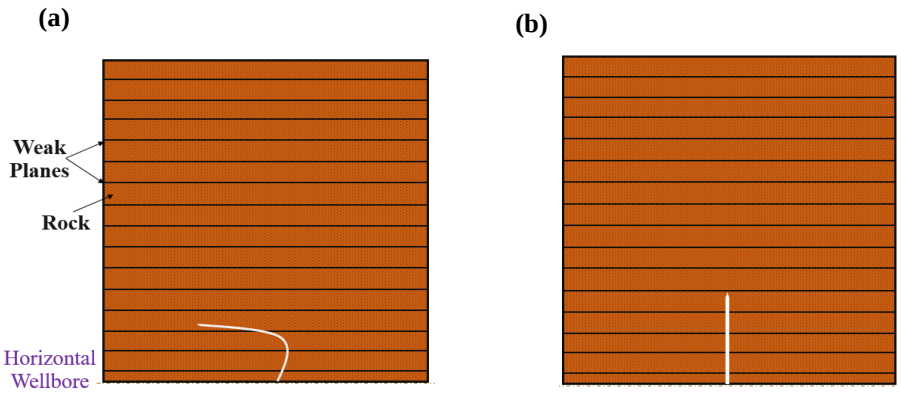


**Figure 31** Crack paths observed in the first study

Moreover, we showed that the fracture permeability can be maintained for a longer period as the spacing between the cracks increases. Using sand proppant in such cases is adequate as long as the value of MC is known. If tight perforations are fired (e.g., 7, 10, 11 m distances), the types of proppants and the method of proppant placement is different. For example, high strength proppants (e.g., ceramic) are suggested due to their ability to minimize crushing, maximizing fracture porosity and permeability, leading to higher production rates (Parker, 2018). The latter

is particularly important in the cases where the horizontal in-situ stress is greater than the vertical one, for example, the Vaca Murata shale formations, where SHmax > Sv. When SHmax > Sv, nonplanar propagation is observed as the side cracks tend to close, which may cause the proppant material to crush and flow out, resulting in poor permeability. The latter is also important in the case of high MCs as the fracture has tendency to close due to the high deviation observed due to the weak planes' presence.

Although the results revealed that wells with tight cluster spacing yield higher fracturing area than the wells with wide cluster spacing, it is worth noting that narrow spacing modes require a higher volume of the injected liquid and proppants (Chakraborty et al., 2017). For tight cluster, the number of perforations is higher than the case of wide cluster spacing so a substantial volume of fluid is needed to allow the cracks to extend.

### 6.3. Conclusion

In this study, the XFEM was used to simulate the HF operation to calculate the injection pressure, fracture geometries and the corresponding permeability and injection pressure. Various injection rates were examined to describe their effects on the geometry of the fracture. The anisotropy was taken into account by treating the reservoir as a VTI medium. The effect of cluster spacing was also studied by analyzing tight and wide cluster spacing (7-20 m) for one and three HF stages and by considering three clusters in each stage. We measured the values of the permeability using a modified version of the Gueguen and Dienes analytical models. The injection rate was found to significantly increase the length, width, and injection pressure in the isotropic medium as the crack will propagate more in length and width as the injection rate increases. In the VTI medium, these variables, however, are strongly dependent on the MC and the value of the injection rate. The crack tends to deviate to the direction of the smallest Young's Modulus when the MC value exceeds 4 and the injection rate is between 1E-4 and 1E-3 $m^3/s$. Cluster spacing was also observed to greatly impact the direction of cracks growth and the permeability. In the isotropic medium and when the distance between the clusters is less than 12 m, the value of the far-field stresses control the crack path as the side cracks (the right and left cracks) propagated away from the

middle crack when $S_{xx} > S_{yy}$ and to the top boundaries when $S_{yy} > S_{xx}$. In the VTI medium, the ratio of the elastic modulus ($E_V/E_H$) dominated as the right, left, and middle cracks tend to kink to the direction of the smallest Young's Modulus. In the multistage HF models, the results reveal that wells with tight clusters provide higher production rates and yield faster pressure depletion. These models provide also an insight about the type of proppants that need to be used in-situ.

### 6.4. Recommendation and Future Work

This study does not include the presence of the natural fracture (NF). The presence of the NF cause the HFs to initiate and propagate along them leading to an increase in the permeability (Rahimi-Aghdam et al. 2019). In addition, the method proposed by Gueguen and Dienes to estimate the permeability does not reflect the permeability of the whole region. The permeability of the whole region might be anisotropic due to the crack orientation. More research needs to be done to accurately estimate permeability evolution using the parameters studied in this study. Finally, the proposed models must be tested with regard to the ductile behavior of formations. Although most of the shales are brittle in nature, some rocks exhibit ductile behavior (ex. Dotternhausen Posidonia shale).

# APPENDIX

## 7.1 Elastic Geomechanical Model

Different elastic models can be used to characterize rock elastic behavior, such as the isotropic model and anisotropic models with their subtypes, namely VTI (Vertical Transverse Isotropy), HTI (Horizontal Transvere Isotropy) and Orthorhombic (Orthotropic) (**Figure 32**). Rock behavior can follow the linear elastic principles when the applied stress is relatively low and the deformations are recoverable. Stress and strain are related by the stiffness tensor as:

$$\sigma_{ij} = C_{ij} * \epsilon_{kl} \qquad ...(15)$$

where , $\sigma_{ij}$ is the stress tensor, and $\epsilon_{kl}$ is the strain tensor, $C_{ij}$ is known as the stiffness tensor which contains 21 constants in the most common anisotropic linear elastic material. Shale formations, however, usually show a symmetry about their vertical axis. This means that the elastic properties are equal in all directions within a horizontal plane, but different in the other directions. The VTI model is, therefore, widely used due to its relative mathematical simplicity, and its ability to provide accurate results for highly heterogeneous rocks (e.g. shales) that cannot be represented in a fully heterogeneous model (Sosa Massaro et al. 2017). An example of this is the Marcellus shale formation in which the horizontal properties are equal while the vertical elastic properties are different(Villamor Lora, Ghazanfari, and Asanza Izquierdo 2016). The stiffness matrix for the VTI rock is given by:

$$C_{ij} = \begin{bmatrix} c_{11} & (c_{11}-2c_{66}) & c_{13} & 0 & 0 & 0 \\ (c_{11}-2c_{66}) & c_{11} & c_{13} & 0 & 0 & 0 \\ c_{13} & c_{13} & c_{33} & 0 & 0 & 0 \\ 0 & 0 & 0 & c_{44} & 0 & 0 \\ 0 & 0 & 0 & 0 & c_{44} & 0 \\ 0 & 0 & 0 & 0 & 0 & c_{66} \end{bmatrix} \quad ...(16)$$

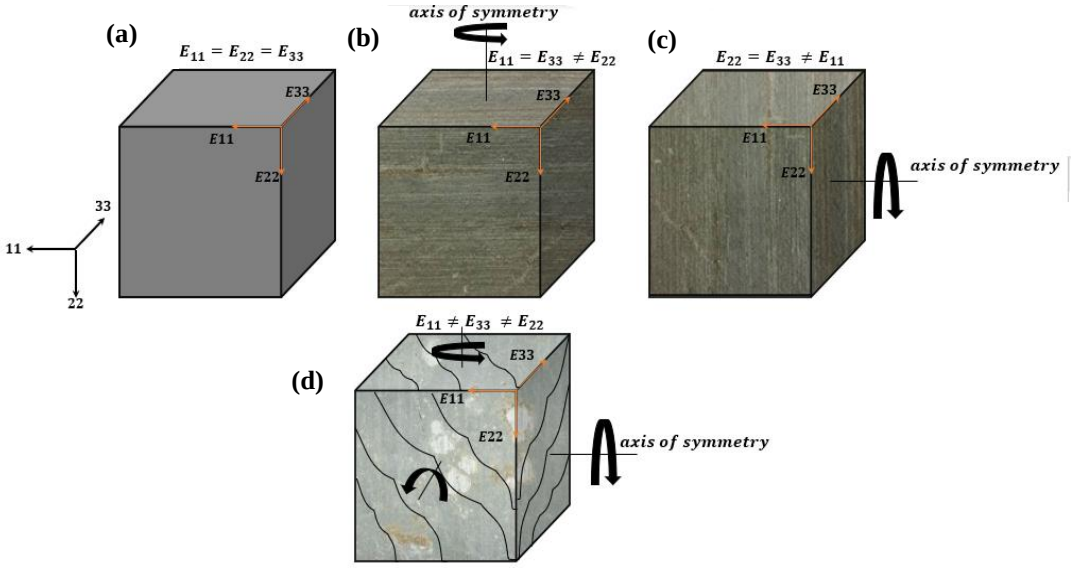


**Figure 32** Anisotropic mechanical models applicable to shale rocks like those found in Vaca Muerta Formation. (a) Basic Isotropic Model, (b) VTI Model, for horizontally laminated rocks; (c) HTI Model, for laminated and steeply dipping rocks (vertical layers); and (d) Orthorhombic Model, for combinations of natural fractures and multi layered rocks. References: VV: Vertical Velocity, VH: Horizontal Fast Velocity and Vh: Horizontal Slow Velocity

# REFERENCES

AlTammar, M. J., Agrawal, S. and Sharma, M. M. (2019) 'Effect of geological layer properties on hydraulic-fracture initiation and propagation: An experimental study', SPE Journal, 24(2), pp. 757–794. doi: 10.2118/184871-PA.

Basin, P., Study, C. and Wells, S. (2017) 'Optimize Completion Design and Well Spacing with the Latest Complex Fracture Modeling & Reservoir Simulation Technologies A Permian Basin Case Study with Seven Wells', (May).

Benzeggagh, M. L. and Kenane, M. (1996) 'Measurement Of Mixed-Mode Delamination Fracture Toughness Of Unidirectional Glass/Epoxy Composites With Mixed-Mode Bending Apparatus', Annales d'endocrinologie, 24, pp. 859–865.

Boone, T. J. and Ingraffea, A. R. (1990) 'A NUMERICAL PROCEDURE FOR SIMULATION OF HYDRAULICALLY-DRIVEN FRACTURE PROPAGATION IN POROELASTIC MEDIA', 14 (September 1988).

Chakraborty, N. et al. (2017) 'Permeability evolution of shale during spontaneous imbibition', Journal of Natural Gas Science and Engineering, 38, pp. 590–596. doi: 10.1016/j.jngse.2016.12.031.

Cheng, Y. and Zhang, Y. (2020) 'Hydraulic Fracturing Experiment Investigation for the Application of Geothermal Energy Extraction'. doi: 10.1021/acsomega.0c00172.

Cui, A., Glover, K. and Wust, R. (2014) 'Elastic and plastic mechanical properties of liquid-rich unconventional shales and their implications for hydraulic fracturing and proppant embedment: A case study of the Nordegg Member in Alberta, Canada', 48th US Rock Mechanics / Geomechanics Symposium 2014, 2(January 2016), pp. 822–833.

Davies, R. et al. (2013) 'Induced seismicity and hydraulic fracturing for the recovery of

hydrocarbons', Marine and Petroleum Geology. Elsevier, 45, pp. 171–185. doi: 10.1016/j.marpetgeo.2013.03.016.

Douma, L. A. N. R. et al. (2019) 'The mechanical contrast between layers controls fracture containment in layered rocks', Journal of Structural Geology. Elsevier, 127(February), p. 103856. doi: 10.1016/j.jsg.2019.06.015.

Erol, S. et al. (2017) 'An Analytical Model of Porosity–Permeability for Porous and Fractured Media', Transport in Porous Media. Springer Netherlands, 120(2), pp. 327–358. doi: 10.1007/s11242-017-0923-z.

Gueguen.Y and Dienes.J (1989) 'Transport Propertie s of Rocks from Statistics and Percolation', International Association for Mathemalical Geology, 1(January).

Haddad, M. and Sepehrnoori, K. (2016) 'XFEM-Based CZM for the Simulation of 3D Multiple-Cluster Hydraulic Fracturing in Quasi-Brittle Shale Formations', Rock Mechanics and Rock Engineering, 49(12), pp. 4731–4748. doi: 10.1007/s00603-016-1057-2.

Li, J. et al. (2019) 'Numerical simulation on deflecting hydraulic fracture with refracturing using extended finite element method', Energies, 12(11). doi: 10.3390/en12112044.

Maji, G. S. V. B. (2018) 'A Study on Crack Initiation and Propagation in Rock with Pre-existing Flaw Under Uniaxial Compression', Indian Geotechnical Journal. Springer India. doi: 10.1007/s40098-018-0304-8.

Maslowski, M., Kasza, P. and Wilk, K. (2018) 'Studies on the effect of the proppant embedment phenomenon on the effective packed fracture in shale rock', (July). doi: 10.13168/AGG.2018.0012.

Mavko, G., Mukerji, T. and Dvorkin, J. (2009) The Rock Physics Handbook. Second Edi.

Modeland, N., Buller, D. and Chong, K. K. (2011) 'Statistical analysis of the effect of completion methodology on production in the Haynesville shale', Society of Petroleum Engineers - SPE Americas Unconventional Gas Conference 2011, UGC 2011, pp. 447–461.

Nasiri, A. (2017) 'A Comparison Study of KGD , PKN and a Modified P3D Model .', (September). doi: 10.13140/RG.2.1.3860.7201.

Rahimi-Aghdam, S. et al. (2019) 'Branching of hydraulic cracks enabling permeability of gas or oil shale with closed natural fractures', Proceedings of the National Academy of Sciences of the United States of America, 116(5), pp. 1532–1537. doi: 10.1073/pnas.1818529116.

Sarkar, S., Toksoz, M. N. and Burns, D. R. (2004) 'Fluid flow modeling in fractures', Earth Resources Laboratory, MIT Earth, pp. 1–41.

Smith, M. (2020) ABAQUS/Standard User's Manual, Version 6.9, Dassault Systemes Simulia Corpia Corp.

Sobhaniaragh, B. et al. (2019) 'Computational modelling of multi-stage hydraulic fractures under stress shadowing and intersecting with pre-existing natural fractures', Acta Mechanica. Springer Vienna, 230(3), pp. 1037–1059. doi: 10.1007/s00707-018-2335-8.

Sosa Massaro, A. et al. (2017) 'Analyzing a suitable elastic geomechanical model for Vaca Muerta Formation', Journal of South American Earth Sciences. Elsevier Ltd, 79(May 2018), pp. 472–488. doi: 10.1016/j.jsames.2017.09.011.

Taylor, P. et al. (no date) 'Petroleum Science and Technology The Experimental Investigation of Fracture Propagation Behavior and Fracture Geometry in Hydraulic Fracturing through Oriented Perforations The Experimental Investigation of

Fracture Propagation Behavior and Fracture Geome', (January 2015), pp. 37–41. doi: 10.1080/10916466.2010.483435.

Villamor Lora, R., Ghazanfari, E. and Asanza Izquierdo, E. (2016) 'Geomechanical Characterization of Marcellus Shale', Rock Mechanics and Rock Engineering, 49(9), pp. 3403–3424. doi: 10.1007/s00603-016-0955-7.

Wang, H. Y. (2015) 'Numerical modeling of non-planar hydraulic fracture propagation in brittle and ductile rocks using XFEM with cohesive zone method', Journal of Petroleum Science and Engineering, 135, pp. 127–140. doi: 10.1016/j.petrol.2015.08.010.

Wang, Y., Li, X. and Tang, C. A. (2016) 'Effect of injection rate on hydraulic fracturing in naturally fractured shale formations: a numerical study', Environmental Earth Sciences, 75(11). doi: 10.1007/s12665-016-5308-z.

Xiong, H. (2018) 'Title Overview'.

XU, Y. et al. (2018) 'Progress and development of volume stimulation techniques', Petroleum Exploration and Development, 45(5), pp. 932–947. doi: 10.1016/S1876-3804(18)30097-1.

Yu, W. and Sepehrnoori, K. (2013) 'Optimization of multiple hydraulically fractured horizontal wells in unconventional gas reservoirs', SPE Production and Operations Symposium, Proceedings, 2013, pp. 476–491. doi: 10.2118/164509-ms.

Zhao, Z. et al. (2016) 'A Laboratory Study of the Effects of Interbeds on Hydraulic Fracture Propagation in Shale Formation'. doi: 10.3390/en9070556.

Zhuang, L. et al. (2019) 'Effect of Water Infiltration, Injection Rate and Anisotropy on Hydraulic Fracturing Behavior of Granite', Rock Mechanics and Rock Engineering. Springer Vienna, 52(2), pp. 575–589. doi: 10.1007/s00603-018-1431-3.

Zielonka, M. G. et al. (2014) ‘Development and Validation of Fully-Coupled Hydraulic Fracturing Simulation Capabilities’, SIMULIA Community Conference, SCC2014, pp. 1–31.